

2012

Calibration of the HAWC Gamma-Ray Observatory

Nathan C. Kelley-Hoskins
Michigan Technological University

Copyright 2012 Nathan C. Kelley-Hoskins

Recommended Citation

Kelley-Hoskins, Nathan C., "Calibration of the HAWC Gamma-Ray Observatory", Master's Thesis, Michigan Technological University, 2012.
<http://digitalcommons.mtu.edu/etds/109>

Follow this and additional works at: <http://digitalcommons.mtu.edu/etds>

 Part of the [Physics Commons](#)

CALIBRATION OF THE HAWC GAMMA-RAY OBSERVATORY

By

Nathan C. Kelley-Hoskins

A THESIS

Submitted in partial fulfillment of the requirements for the degree of

MASTER OF SCIENCE

(Physics)

MICHIGAN TECHNOLOGICAL UNIVERSITY

2012

© 2012 Nathan C. Kelley-Hoskins

This thesis, "Calibration of the HAWC Gamma-Ray Observatory," is hereby approved in partial fulfillment of the requirements for the Degree of MASTER OF SCIENCE IN PHYSICS.

Department of Physics

Signatures:

Thesis Advisor _____
Dr. Petra Huentemeyer

Committee Member _____
Dr. Brian Fick

Committee Member _____
Dr. Alex Kostinski

Committee Member _____
Dr. Allan Struthers

Department Chair _____
Dr. Ravi Pandey

Date _____

To my mother, teachers and friends

who didn't hesitate to criticize my work at every stage - without which I'd neither be who

I am nor would this work be what it is today.

Contents

List of Figures	xi
List of Tables	xiii
Acknowledgments	xv
Abstract	xvii
1 Introduction	1
1.1 Gamma-Ray Astronomy	1
1.2 Science Objectives	4
1.3 Gamma-Ray Showers	6
1.4 Gamma Ray Detectors	8
1.4.1 IACT Detectors	8
1.4.2 Surface Particle Detectors	9
2 HAWC	11
2.1 Observatory	11
2.2 Gamma Ray Reconstruction	14

2.3	Energy Sensitivity and Altitude	16
3	Calibration System	21
3.1	Hardware	21
3.1.1	Laser System	22
3.1.2	Calibration Layout	24
3.1.3	PMT Network	25
3.1.4	RTT Network	28
3.1.5	Interface with Data Acquisition System (DAQ)	29
3.1.6	Radiometer Usage	30
3.2	Control Software	31
3.2.1	Daemon	32
3.2.2	Sockets	33
3.2.3	Interface with Experiment Control	35
3.2.4	Drivers	38
3.2.5	Tasks	39
3.2.5.1	Radiometer Ranging Task	41
3.2.5.2	Slewing Task	42
4	Systematic Studies	47
4.1	Pulsing Frequency	48
4.2	Radiometer Triggering Modes	50
4.3	Filter Wheel Repeatability	52

4.4	Temperature Dependence	54
4.5	Multifiber Testing	55
4.6	Radiometer Range Determination	59
5	Conclusion	63
	References	65
A	Software	69
B	Calibration Hardware	71
B.1	Laser	71
B.2	Laser Power Supply	72
B.3	Filter Wheel	72
B.4	Pulser	73
B.5	Timing Counter	73
B.6	Fiber Optic Switch	74
B.7	Milagro Fiber Optic Switch	74
B.8	Radiometer	74
B.9	LabJack DAQ Board	75

List of Figures

1.1	Cosmic Ray Flux	2
1.2	Life of a Gamma Ray	3
1.3	Gamma Ray Shower Particle Graph	7
1.4	VERITAS Detector	9
1.5	Aerial View of the Milagro detector	10
2.1	HAWC Tank and PMT Layout	12
2.2	Effect of Cables on PMT Output Signal	13
2.3	PMT and WCD Bladder	13
2.4	PMT Signal Digitization	15
2.5	Angular Reconstruction Diagram	15
2.6	HAWC diagram of a gamma ray shower	17
2.7	HAWC Energy Sensitivity	18
2.8	HAWC Effective Area	19
3.1	Laser	22
3.2	R5912 Spectral Response	23
3.3	Basic Calibration Layout	25

3.4	Calibration Layout	26
3.5	550ft Fiber Layout	26
3.6	Tank Distribution Box	27
3.7	Diffuser	27
3.8	Slewing Plot	44
4.1	Laser Shot Energy vs Pulsing Frequency	48
4.2	Random Multiple Pulsing Frequency	49
4.3	Triggering Plot	51
4.4	Detail Plot of Bad Trigger	51
4.5	Filter Wheel Optical Depths	52
4.6	Filter Wheel Optical Depth Ratings	54
4.7	Pulse Energy vs Temperature	54
4.8	No Teflon	56
4.9	CCD Image of Beam Profile	57
4.10	Teflon Plot	58
4.11	Radiometer Range Limit	59
4.12	Radiometer Digital Limit	61

List of Tables

3.1 Table of CalDaemon states 33

B.1 Optical Depth of Filter Wheel Filters 72

Acknowledgments

I would like to thank all those who have helped me learn, understand and appreciate this subject as well as those who helped me with L^AT_EX 2_ε -

Abstract

The High-Altitude Water Cherenkov (HAWC) Experiment is a gamma-ray observatory that utilizes water silos as Cherenkov detectors to measure the electromagnetic air showers created by gamma rays. The experiment consists of an array of closely packed water Cherenkov detectors (WCDs), each with four photomultiplier tubes (PMTs). The direction of the gamma ray will be reconstructed using the times when the electromagnetic shower front triggers PMTs in each WCD. To achieve an angular resolution as low as 0.1 degrees, a laser calibration system will be used to measure relative PMT response times. The system will direct 300ps laser pulses into two fiber-optic networks. Each network will use optical fan-outs and switches to direct light to specific WCDs. The first network is used to measure the light transit time out to each pair of detectors, and the second network sends light to each detector, calibrating the response times of the four PMTs within each detector. As the relative PMT response times are dependent on the number of photons in the light pulse, neutral density filters will be used to control the light intensity across five orders of magnitude. This system will run both continuously in a low-rate mode, and in a high-rate mode with many intensity levels. In this thesis, the design of the calibration system and systematic studies verifying its performance are presented.

Chapter 1

Introduction

1.1 Gamma-Ray Astronomy

Gamma-ray astronomy is the science of detecting photons above 1 MeV, or gamma rays, from different places in our universe. As high-energy physical processes are needed to create gamma rays, gamma-ray astronomy can be used to locate and study some of the most violent events in outer space.

Before the 1960's, astronomy was done in other electromagnetic wavelengths like infrared, visible, and radio, but these photons are created by lower-energy physics, leaving higher-energy processes unstudied. After the 1960's, telescopes were built that could detect gamma rays, both on the ground and on satellites.

While satellite experiments can measure gamma rays with energies as high as hundreds of GeVs[2], ground-based detectors are needed to measure gamma rays above these energies. The reason is that cosmic-ray and gamma-ray fluxes generally decrease exponentially with energy, as shown in Figure 1.1, and larger

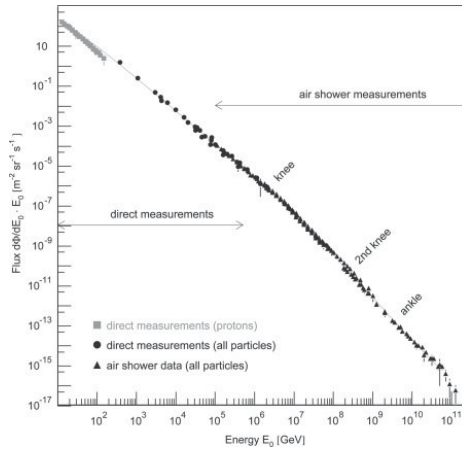


Figure 1.1: Cosmic Ray Flux. Gamma rays comprise 0.1% of the flux.[1]

detector areas are needed to be able to make statistically significant measurements.

Gamma-Ray astronomy involves more steps than conventional radio or optical astronomy, due to the atmosphere being opaque to gamma rays, whereas it is transparent to various other wavelengths. The process can be summarized in eight steps that are illustrated in Figure 1.2 and will be described in more detail in the following subsections.

1. A gamma ray is created through a high-energy event.
2. The gamma ray then travels through space, and eventually collides with the Earth.
3. After passing through part of the atmosphere, the gamma ray interacts with a molecule in the air, and an electron-positron pair is produced.
4. The electron and positron then interact with other molecules in the air, producing more secondary particles. These interactions repeat many times, creating many

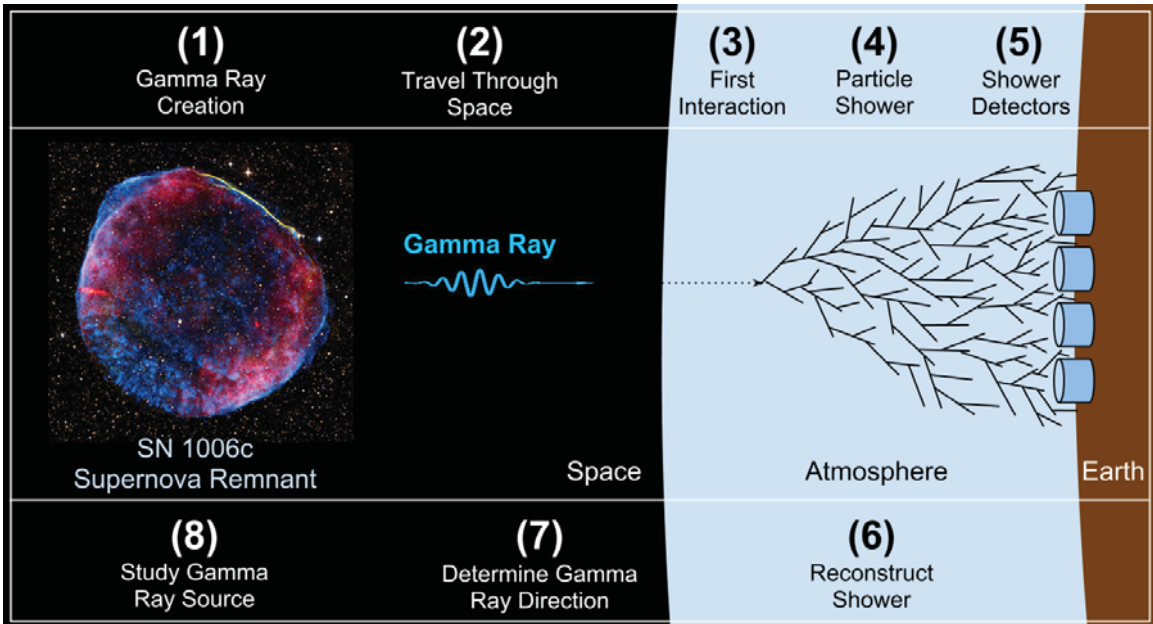


Figure 1.2: The Anatomy of Gamma-Ray Astronomy.

particles in a particle shower, called an Extensive Air Shower (EAS).

5. Particle detectors on Earth then detect the particle shower. The particle shower can be detected with the air Cherenkov technique as it progresses through the atmosphere, or with the particle-sampling technique using a ground array of particle detectors, such as water Cherenkov counters.
6. Using fast electronics, custom-designed Data Acquisition Systems (DAQs), and reconstruction software, the shower is reconstructed, quantifying the shower in characteristic observables.
7. The original gamma-ray time-of-arrival is recorded and its direction and energy are determined, using custom-designed analysis and simulation software.
8. The spectral energy distribution, time dependence, and morphology of gamma

emission from sources that are identified in the previous steps are studied in order to shed light onto the particle production and acceleration mechanisms that occur in the sources.

1.2 Science Objectives

Gamma rays are created by a number of sources that can be studied with data from a Gamma-Ray Observatory. Within our galaxy, supernova remnants, pulsars, binary systems, and cosmic ray interactions with interstellar matter and radiation fields (diffuse emission) can create gamma rays, while outside of our galaxy, Active Galactic Nuclei (AGN) and Gamma-Ray Bursts (GRBs) are sources of gamma rays.

Supernova remnants can accelerate protons beyond gamma-ray energies. These accelerated protons, or Cosmic Rays (CRs) then interact with nearby matter, producing π^+ , π^- , and π^0 mesons, where the π^0 quickly decays into two gamma rays. Another method of gamma-ray production involves electrons that, after they are accelerated in a source, interact with low-energy photons of the cosmic microwave background or infrared radiation fields. Through inverse Compton scattering, these low-energy photons acquire energy from the electrons, turning them into TeV gamma rays. These two processes are the dominant production mechanisms for very high energy gamma rays.

TeV gamma rays are produced in two main regions of pulsar wind nebula. First, a pulsar's ultra-relativistic jets can produce very narrow spectra of gamma rays, in the range of 10 GeV to 1 TeV.[3] Second, a shock region is formed when the ultra-relativistic jets collide with nearby matter. This shock region can produce gamma rays up to and beyond 100 TeV.

In the third region close to the pulsar, it was thought that the strong magnetic fields would suppress any TeV gamma rays. In 2011 though, the VERITAS detector discovered pulsed gamma rays above 100 GeV from the Crab Pulsar. The pulsed nature of these gamma rays indicates the production region is close to the pulsar, with a minimum radius of 10 stellar radii from the pulsar.[4]

Another source of TeV gamma rays are binary systems. These systems are made up of either a) a pulsar and another star, or b) a microquasar (stellar-mass black hole) and another star. Both expel large amounts of energy through relativistic jets from the pulsar/microquasar, but the addition of a second star in the vicinity of the jet alters the TeV spectra from these sources, making them different from lone quasars or lone pulsars.

Diffuse-emission gamma rays are created when cosmic rays (protons) interact with matter in between stars in our galaxy. This leads to a dim haze of gamma rays along the plane of our galaxy. By studying diffuse emission spectra, estimates can be made about cosmic ray spectra at various locations in our galaxy.

Outside our galaxy, Active Galactic Nuclei (AGN) are gamma-ray sources. They are

objects with a supermassive black hole at their center. Due to a large amount of matter that they consume, they produce large amounts of electromagnetic radiation across many wavelengths, and jets of relativistic material along their poles. AGNs are classified according to the directions of their jets with respect to Earth. AGNs with relativistic jets close to the line of sight are called blazars. Blazars are known TeV gamma-ray emitters. The jets create TeV gamma rays through inverse Compton scattering and CR-pion decay. By studying the spectra and time variability of the TeV gamma rays, properties of AGNs can be determined.

Another source of TeV gamma rays are Gamma-Ray Bursts (GRBs). These are bright gamma-ray flashes that have durations from milliseconds to minutes, and come from locations outside our galaxy. All-sky survey instruments can detect the initial flash of a GRB, and alert other telescopes so that they can point towards the location and measure the afterglow of the GRB.[3]

1.3 Gamma-Ray Showers

As mentioned before, TeV gamma rays are studied through the detection of Extensive Air Showers (EASs) represented by steps 3-6 in Figure 1.2.

Because the path length of a gamma ray is short compared to the thickness of the

atmosphere, the gamma ray itself does not reach the surface of the Earth. Instead, it usually interacts electromagnetically with an air molecule, and is converted into an e^+ and e^- pair, as illustrated in Figure 1.3.

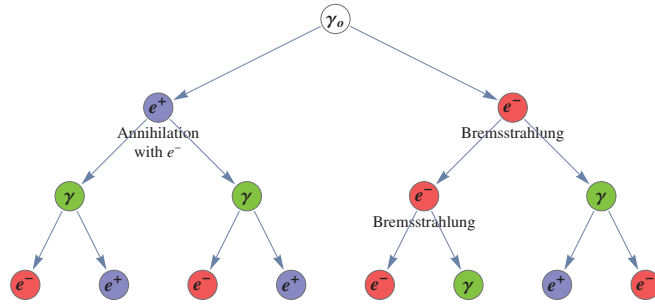


Figure 1.3: Gamma Ray Shower Particle Graph. The initial gamma ray γ_0 starts the shower, which spreads its energy out into other gamma rays, e^+ 's, and e^- 's.

These 1st-generation e^+ and e^- travel through the atmosphere, where the electron loses some energy via Bremsstrahlung, which creates more photons, and the positron annihilates with another e^- in the atmosphere, producing two gamma rays. These processes repeat many times, distributing the original gamma ray energy across many particles. The particle multiplication stops when the average electron energy drops below about 80 MeV, the critical energy. Below this energy, the shower slowly decays because the electrons predominantly lose their energy through ionization and the photons through Compton scattering, thus not producing any more particles.

The front of an EAS is a single “curved-pancake” wave of e^+ s, e^- s, and γ s several meters thick and 100s of meters wide, which travels for kilometers through the atmosphere over a time span of μ s before it strikes the detector array.

1.4 Gamma Ray Detectors

Gamma-ray detectors can be roughly divided up into two groups based on the parts of the shower they detect. Imaging Atmospheric Cherenkov Telescopes (IACTs) are described in section 1.4.1. They take images of the Cherenkov light that is emitted by the EAS as it travels through the atmosphere. Surface particle detectors are described in section 1.4.2, which detect the gamma-ray shower particles as they strike the surface of the Earth using the particle-sampling technique.

1.4.1 IACT Detectors

Imaging Atmospheric Cherenkov Telescopes (IACTs) detect photons created by the EAS, similar to camera taking a picture of a lightning strike. The photons that are detected are created via the Cherenkov process. The detectors are operationally very similar to optical telescopes. They can only function on moonless nights, which results in a very short duty cycle (10%). They also have a small field of view ($<10^\circ$), and are operated by pointing at a specific observation target to detect gamma rays. The primary sensing elements are usually Photomultiplier Tubes (PMTs) augmented by a mirror. Examples of IACTs include VERITAS[5], HESS[6], and MAGIC[7], and Whipple[8].



Figure 1.4: The four telescopes of the VERITAS Detector.

1.4.2 Surface Particle Detectors

The second group of TeV gamma-ray experiments detect the shower particles as they hit the surface of the Earth and travel through elements of the detector, which are spread out over an area of 100's m^2 . The primary sensing element varies from detector to detector, but can include PMT's viewing a Cherenkov or scintillation medium, resistive plates, or other kinds of detectors.

Since this detector type does not rely on optics that are exposed, it is not limited by the sun or moon, and can in principle operate all the time. This makes this detector type ideal for studying time-dependent gamma-ray sources, or for searching for hither-to unknown sources. As most surface particle detectors can detect particles coming in from any direction, they are able to observe a large area of the sky all at once. On the other hand, IACTs have a much better angular and energy resolution because an IACT takes images of

the shower as it propagates through the atmosphere.

Milago[9], IceCube[10], Cascade[11], and Tunka[12] are examples of surface particle detectors. In Figure 1.5, the centerpiece of the Milagro detector can be seen, an 8 by 60 by 80 m^3 pond filled with purified water and instrumented with two layers of 723 PMTs.



Figure 1.5: Aerial view of the Milagro detector.

In the following chapter a new TeV gamma-ray observatory named the High Altitude Water Cherenkov (HAWC) Observatory will be described. This observatory uses the particle-sampling technique, and is currently under construction in Mexico.

Chapter 2

HAWC

The High Altitude Water Cherenkov (HAWC) observatory is a TeV gamma-ray observatory currently under construction in Mexico. Section 2.1 will discuss the configuration of the observatory, including the Water Cherenkov Detectors (WCDs) and the Photomultiplier Tubes (PMTs). Gamma-ray reconstruction methods will be discussed in Section 2.2. In Section 2.3, the (energy) sensitivity of the HAWC observatory will be discussed.

2.1 Observatory

The HAWC observatory is being built on the slopes of Pico de Orizaba in Mexico at an altitude of 4100 meters. The HAWC observatory will consist of 250 Water Cherenkov

Detectors (WCDs). Each WCD is a cylindrical water silo 7.3 m in diameter, with a water depth of 4.5 m. Each WCD contains four upward-facing PMTs at the bottom of the WCD, which are connected to ~ 180 m analog high voltage cables.

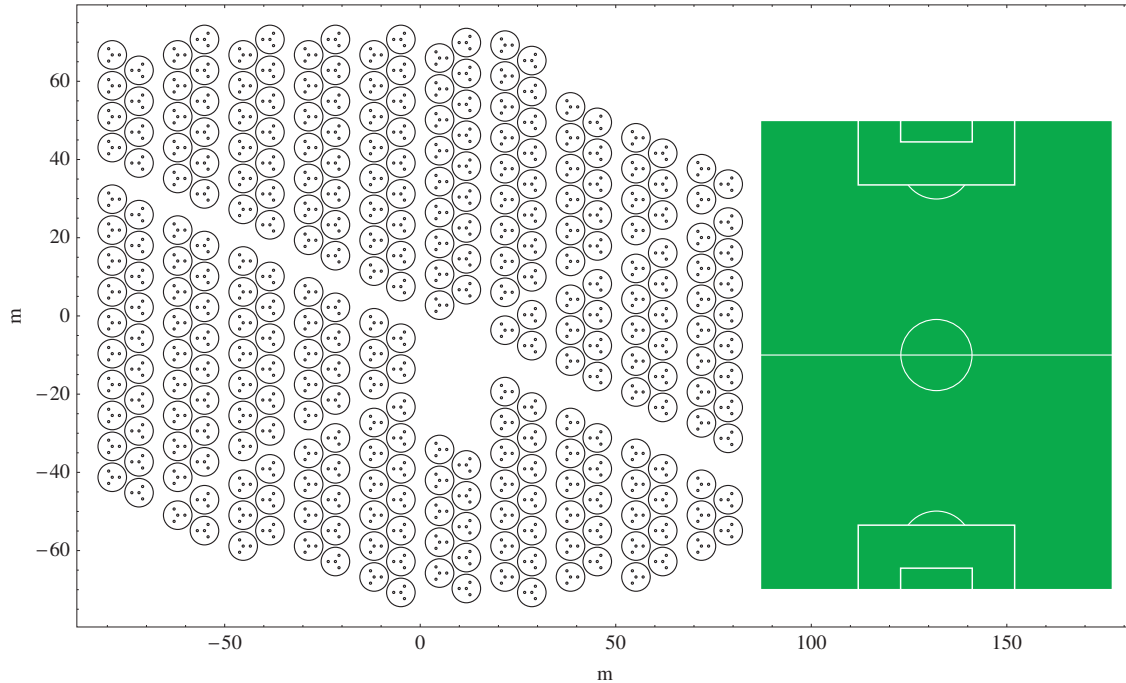


Figure 2.1: HAWC Array Layout and PMT Positions. Large circles denote WCD positions and radii, dots represent PMT positions within each WCD. A soccer field is included for scale.

The cables are connected to a series of electronic devices for digitizing the analog voltage signal from the PMTs. It is important to note that the combination of the PMT and its 180 meter cable is the complete sensor, and not just the PMT. The PMT signals are not digitized at the PMT. The signals from the PMT (voltage pulses with a width of around ~ 10 's of nanoseconds) travel down the cable and thus get dispersed, so that at the end of the cable they are around hundreds of nanoseconds wide. The effect of this signal dispersion is illustrated in Figure 2.2.

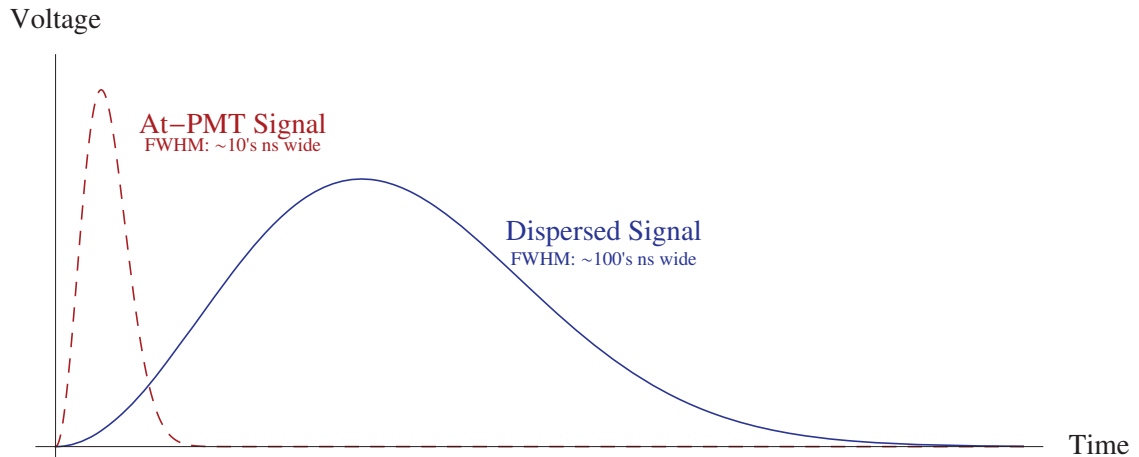


Figure 2.2: Time dependence of the voltage of a PMT signal before and after the dispersion effects of a 200m cable. Output PMT voltage in Red (dashed), measured at the PMT. The same signal after dispersion is in blue (solid).

The PMTs have a reflective baffle collar to increase their effective area, and are run at a voltage of around 1600 Volts. The WCDs are closely packed, and the whole observatory covers an area of 20,000 m², as is illustrated in Figure 2.1.



Figure 2.3: A PMT and a bladder used in the observatory.

The three outer PMTs are 8" Hamamatsu R5912 PMTs[13] arranged in a triangle around

the central vertical axis of the WCD. The fourth (center) PMT is a high-efficiency Hamamatsu R7081 PMT[14]. Each WCD will contain its water in an air-, water-, and light-tight bladder made of PVC (XR3 PW) material.[15]

At the end of the 180 meter cable, the signal from the PMTs are digitized by a set of two-threshold TDCs[16], which feed the digitized signal to computers for analysis. As the digitization needs to have a high temporal bin size (0.1 ns), and must handle a high frequency of signals (20khz), specialized electronics are used to convert the analog voltage signal from the PMTs to binary data. The primary digitization circuit has two voltage thresholds, and outputs “0” when outside the thresholds, and “1” when between the thresholds as explained in [17], page 33. This digitization can be seen in Figure 2.4. Each “0” or “1” represents 0.1 ns of time, and the thresholds are set to a voltage roughly corresponding to 0.5 photoelectrons (PEs) and 4 PEs.

2.2 Gamma Ray Reconstruction

The original gamma-ray direction can be defined by its zenith and azimuth angle with respect to the detector. These angles can be calculated by measuring the time difference between the PMT signals from neighboring WCDs. A larger average time difference indicates that the shower came in at a lower zenith angle, while a smaller time difference indicates a higher zenith angle.

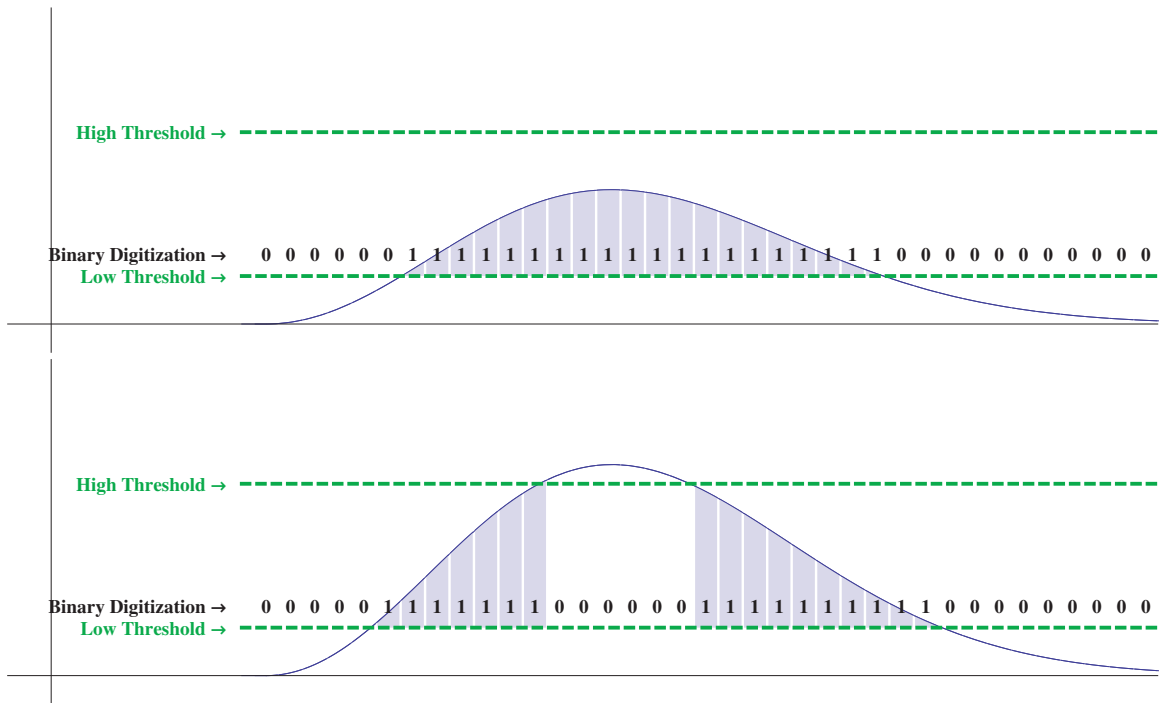


Figure 2.4: Digitization of the output voltage signal from a PMT.

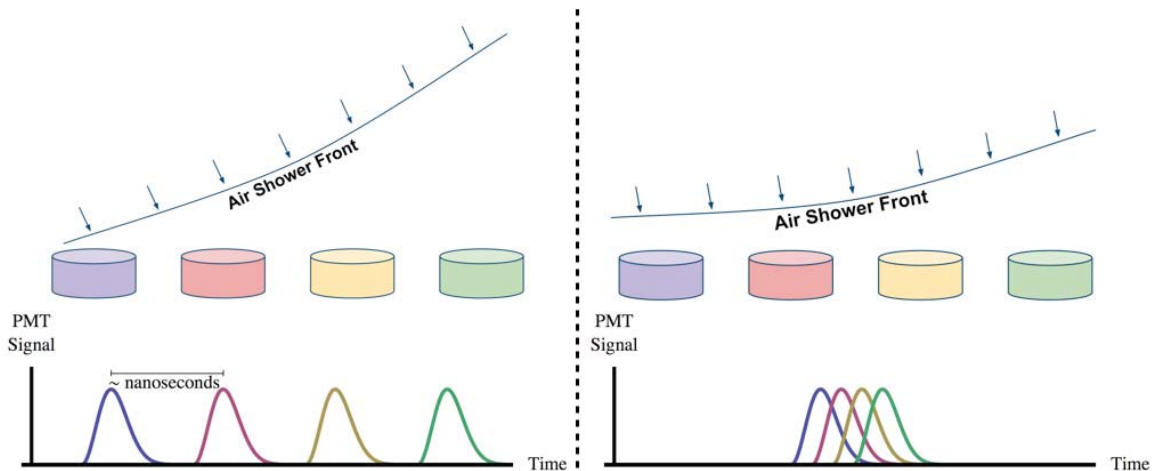


Figure 2.5: 2D Angular Reconstruction Method Example.

In Figure 2.5, a two-dimensional example of this is shown. On the left, a gamma ray shower comes in at a low angle ($\sim 55^\circ$). As the WCDs are spread out horizontally, this means that the shower front reaches each WCD at a different time, with a time difference

between WCD signals on the order of 10 ns. On the right, a similar shower instead comes in almost overhead, and it can be seen that, due to the nearly flat nature of the shower front, the difference between WCD signals is much less. In order to reconstruct the zenith angle of a gamma-ray shower with an accuracy of less than $\sim 0.5^\circ$, the observatory must possess a relative timing accuracy of less than 1 ns between neighboring WCDs.

Figure 2.6 shows a simulation of a shower front detection in the HAWC array. The color of different tanks indicates the time the shower hit that WCD. The shower direction corresponds to the connecting line between the first- and last-hit tanks. An iterative fit to the PMT signal times and strengths is used to reconstruct the angle of an event.

The energy of a gamma-ray roughly corresponds to the number of PMTs that were triggered. However, since a gamma ray could have interacted earlier or later in the atmosphere, the plane of a Surface Particle Detector may take a slice of the shower earlier or later, which will change the number of triggered detectors. This effect is usually the largest contribution to the uncertainty of energy measurements with Surface Particle Detectors.

2.3 Energy Sensitivity and Altitude

The point source sensitivity of the HAWC array between 1 and 100 TeV is shown in Figure 2.7, in comparison to other detectors. The dashed line shows the sensitivity after one year

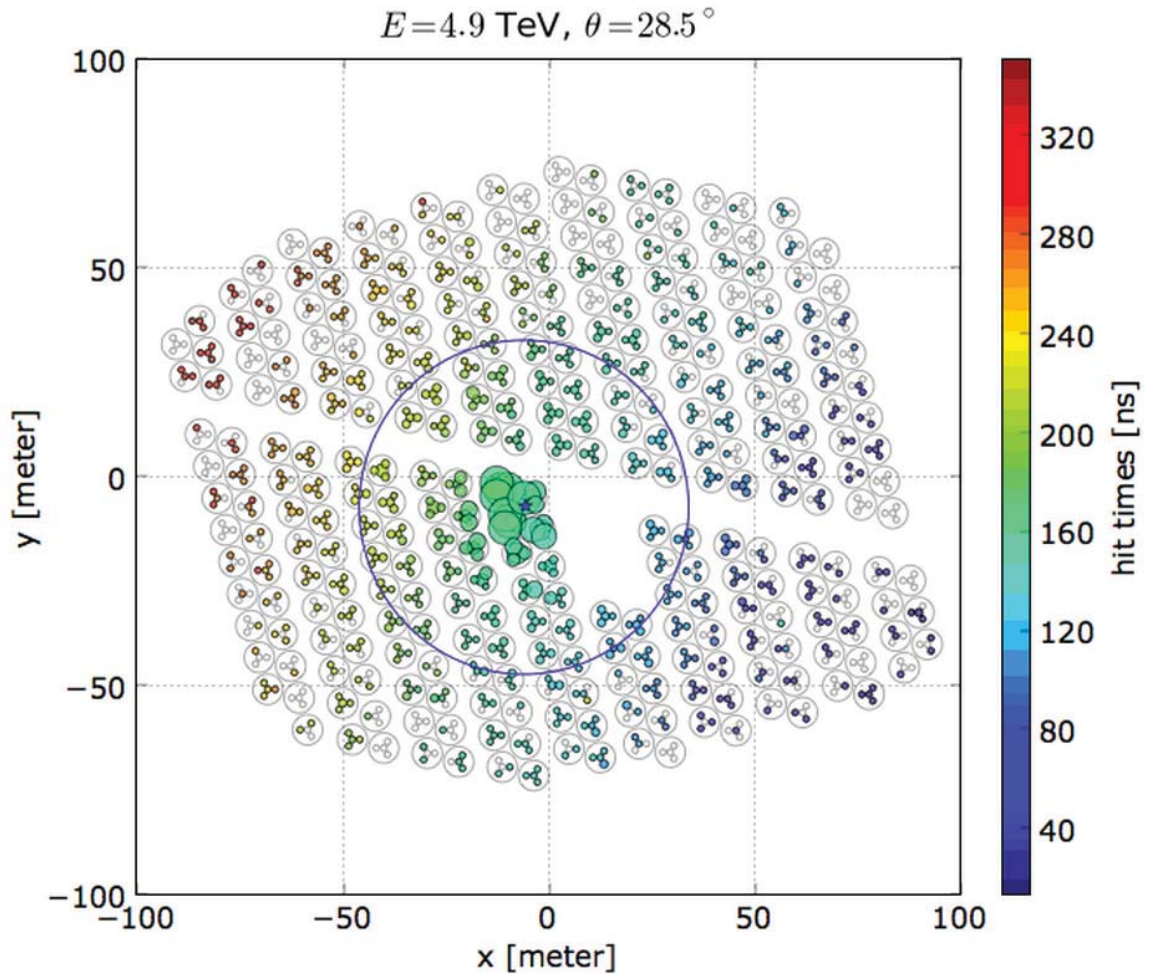


Figure 2.6: A simulated air shower as seen by the HAWC detector. PMTs colored according to when they were struck by the shower front. The initial gamma ray had an energy of 4.9 TeV, and struck the array at an angle of 28.5° from the vertical.

of data taking, the solid line after five years. The upper energy range is limited by the flux spectra of gamma rays. As there are fewer higher energy gamma rays, the area of the detector becomes too small to detect a significant number of them. A similar effect occurs at the low energy limit, where gamma-ray showers are smaller and do not propagate as far through the atmosphere.

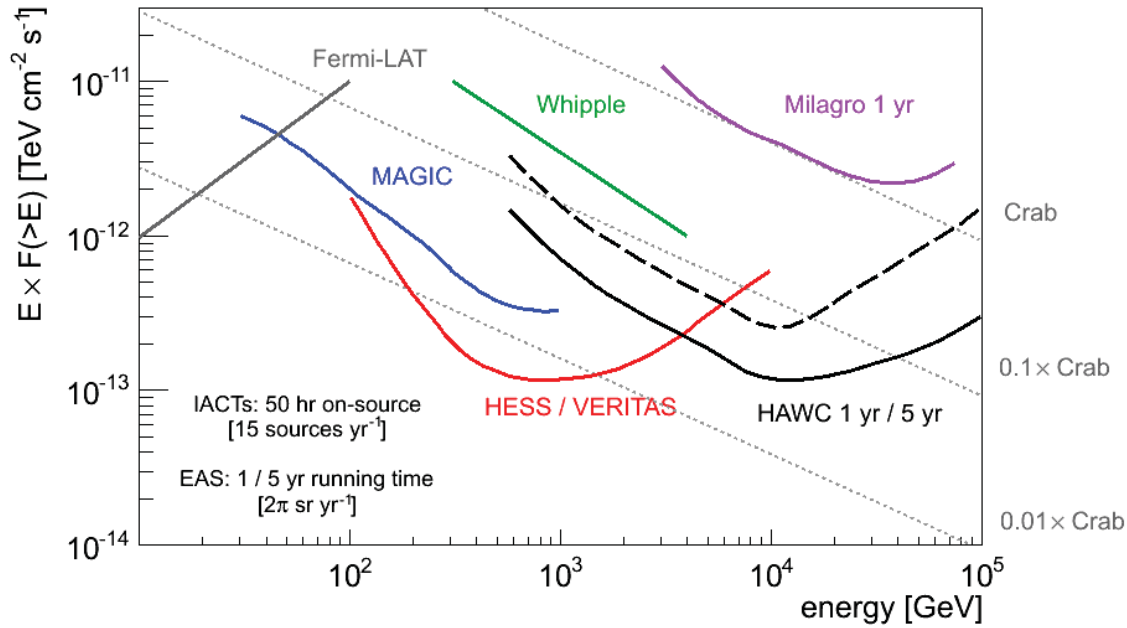


Figure 2.7: Sensitivity of the HAWC array as a function of incident gamma ray.

HAWC is being built at an altitude of 4100m above sea level, to increase its gamma-ray sensitivity. In Figure 2.7 Milagro is shown to have a lower energy limit near 1 TeV, while HAWC will be ~ 15 times more sensitive than Milagro.

In Figure 2.8, the effective area of the HAWC observatory is shown. At gamma-ray energies around 100GeV, a gamma-ray shower strikes an area of the detector measuring approximately 100m^2 , while a 100TeV gamma-ray shower strikes a larger area of the detector, measuring around $10,000\text{m}^2$. The high-altitude placement of the HAWC observatory is partially responsible for the improvement in the effective area for low energy gamma rays.

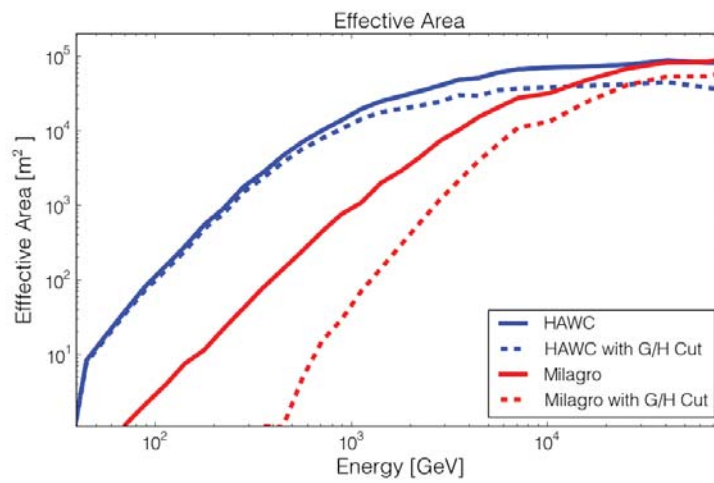


Figure 2.8: The effective area of HAWC with respect to gamma-ray energy. The dashed lines represent the effective area after applying a Gamma/Hadron cut to the monte carlo data.

Chapter 3

Calibration System

The calibration system consists of a laser system, several fiber-optic networks, and a control computer running custom software to manage all equipment. The purpose of the calibration system is to record calibration data in a stable and repeatable manner over the lifetime of the observatory. Section 3.1 discusses the hardware of the calibration system, while section 3.2 discusses the control software that has been developed.

3.1 Hardware

This section details the different hardware used in the calibration system. This includes the central laser system in Subsection 3.1.1 featuring a pulsed laser, and the overall layout of

the calibration system in Subsection 3.1.2. Several fiber-optic networks are discussed in Subsections 3.1.3 and 3.1.4, and the usage of multiple radiometers is discussed in section 3.1.6. The interaction between the Calibration system and the main DAQ is covered in Subsection 3.1.5.

3.1.1 Laser System

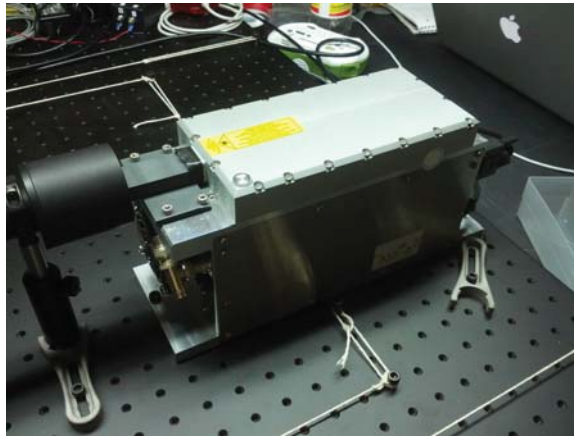


Figure 3.1: The Laser.

The centerpiece of the calibration system is a 532nm pulsed laser. It fires 300 ps long pulses of an energy of ~ 45 uJ with frequencies between 10 Hz and 500 Hz, and has a beam area of ~ 0.5 cm² [18].

Its purpose is to simulate the light signal created by the air shower front as it passes through the detector. The laser has three key properties, which are chosen to facilitate the calibration process. A wavelength of 532 nm is chosen for several reasons. First, there is a tradeoff between the PMT quantum efficiency and the fiber-optic cable transmission efficiency.

The fiber-optic cables are commercially designed for infrared wavelengths, with decreased transmission efficiency at other wavelengths, resulting in $\sim 1\%$ transmission efficiency for green wavelengths. Conversely, the PMT quantum efficiency peaks at 25% for blue wavelengths, but green wavelengths have a reduced quantum efficiency of 8%, as shown in 3.1.1.

Second, the laser pulse width needs to be much less than the thickness of the shower, which is around 2m, or 10ns. Since the purpose of the calibration system is to find the response time of the PMTs, the arrival time of the photons within the laser pulse must possess a similar time scale as the digitization electronics. If it is not, the PMT could detect a photon from the beginning of the pulse, or from the end, introducing uncertainty in the PMT response time.

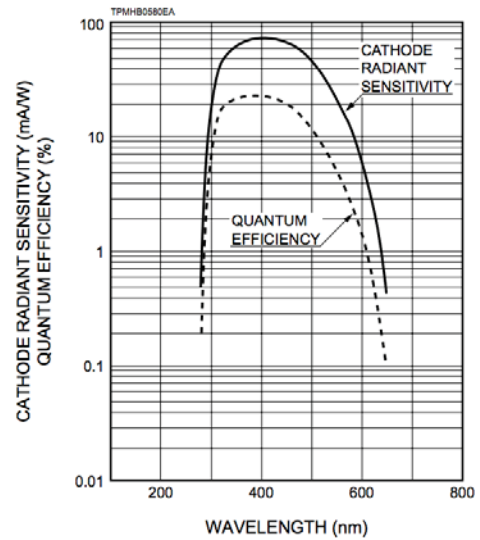


Figure 3.2: Spectral Response of a typical R5912 PMT.[13]

The third required property for the laser is that it produces pulses of photons with an energy of 45 uJ. This energy ensures that the light intensity arriving in the WCDs is sufficient to calibrate the PMTs between 0.1 PEs to 10,000 PEs after the light has passed through a network of up to 200m long fibers.

Diffusers and beam expanders are used, so that the light directed to the PMTs is less

affected by details of the beam shape and speckling effect and therefore is stable over time. This allows for a system which is not greatly affected by vibrations in the optical table or local temperature changes, while still producing enough photons to reach the detectors.

Another requirement of the calibration system is to create laser pulses with a variety of energies that correspond to PMT signals between 0.1 and 10,000PEs. This is achieved by using three filter wheels[19] to hold neutral density (ND) filters in place that combine to optical depths between 0.0 and 7.0. The three filter wheels in series can produce 125 different light levels.

3.1.2 Calibration Layout

The calibration system consists of a number of pieces of equipment which are used in the laser system and the fiber-optic networks.[20] An illustration of all the equipment is shown in Figure 3.3. The primary components that connect to the laser system are the PMT fiber-optic network (PMT network) and the Round-Trip-Timing Fiber-Optic network (RTT network). The PMT network, which routes laser pulses to the PMTs, is designated by the red lines in Figure 3.3, and is described in Subsection 3.1.3. These light pulses are used to measure the PMT response time, though the “time” this network measures includes the time the pulse spent in the fiber. To measure and remove the time spent in the fiber, the RTT network is used. This network is designated by the blue lines in Figure 3.3, and

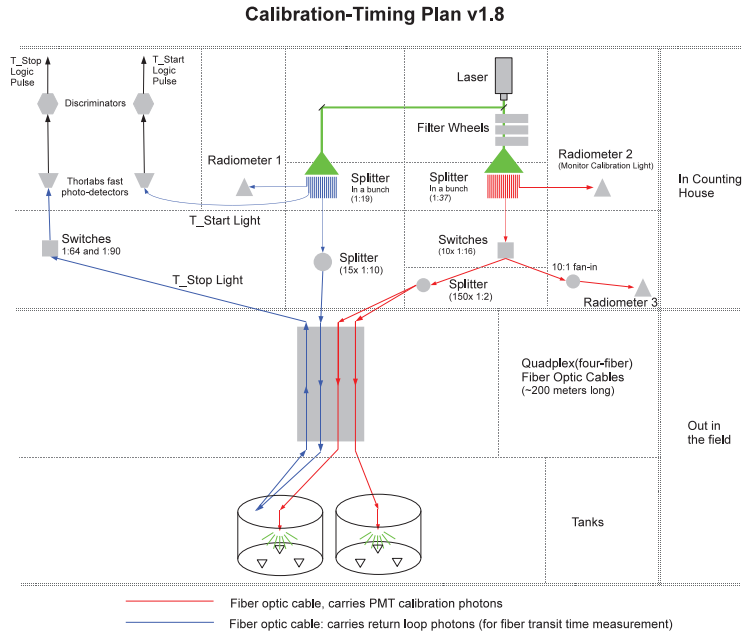


Figure 3.3: Simple Layout of the calibration system. Red fibers feed laser pulses directly into WCDs, blue fibers are used for round-trip-time measurements.

is described in Subsection 3.1.4. Each pair of WCDs is serviced by a single cable, which contains four fibers. Two of these fibers are used by the PMT network, while the other two fibers are connected together, forming one of the loops used in the RTT network.

3.1.3 PMT Network

The purpose of the PMT fiber-optic network is to carry laser pulses from the laser apparatus to the diffusers inside the WCDs. These pulses can be varied in their intensity, allowing PMT response times to be measured from 0.1 PE to 10,000 PE. In Figure 3.4, the PMT network starts with a fiber-optic splitter, Splitter 3. Splitter 3 consists of a 1:22 fiber-optic

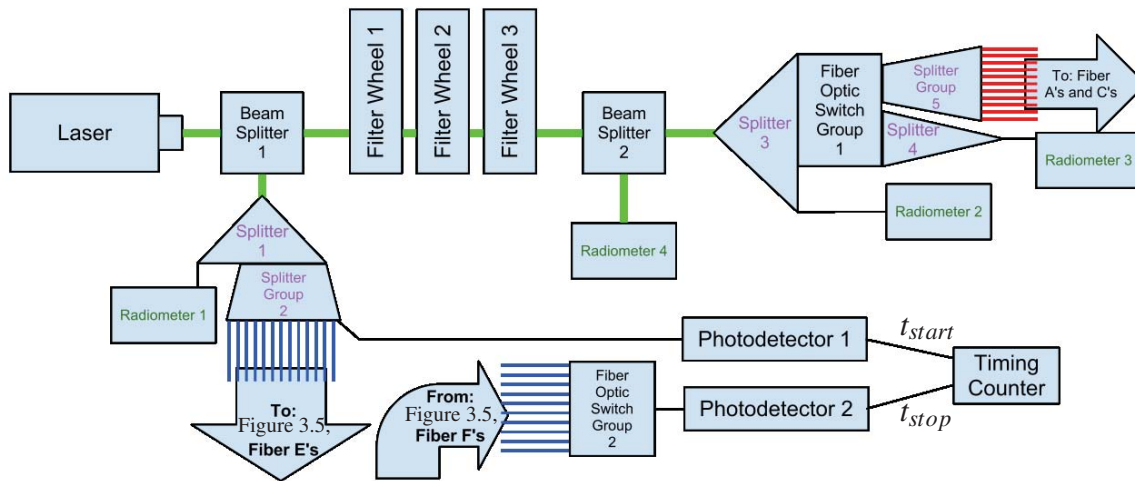


Figure 3.4: Detailed view of the layout of the calibration network. Blue lines are fibers used in the timing fiber-optic network, Red lines are fibers used in the PMT fiber-optic network. Fiber's A, C, E and F are diagrammed in Figure 3.5. Light green lines represent the path of the laser, and black lines represent single fiber-optic cables.

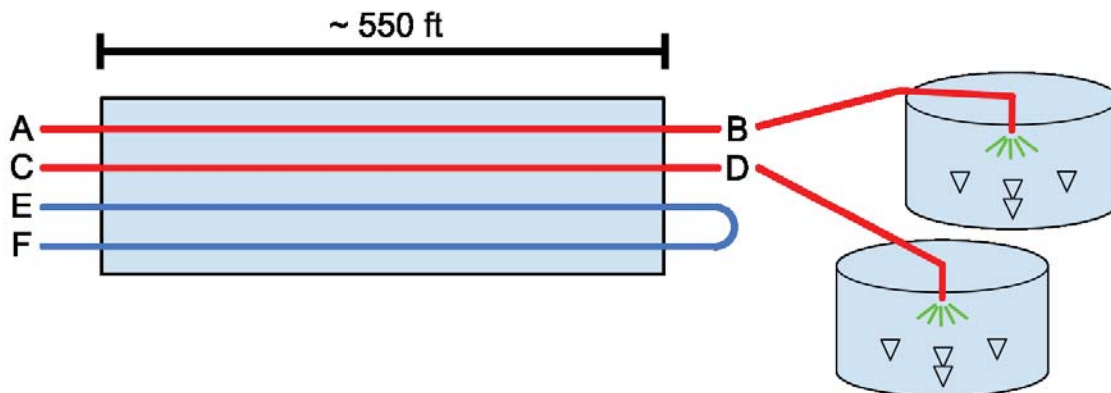


Figure 3.5: Layout of the 550 ft cable. Red fibers feed laser pulses directly into detectors, blue fibers are used for round-trip-time measurement.

splitter. One fiber from Splitter 3 is fed to Radiometer 2, while 10 other fibers are connected to Switch Group 1, which consists of 10x 1:16 fiber-optic switch modules.

On each switch module, outputs 1-15 are connected to Splitter Group 5, a layer of 150x 1:2 splitters. The outputs of Splitter Group 5 are 300 fiber-optic cables, each of which are

connected to the fibers A and C of the 150x 550ft cables, as diagrammed in Figure 3.5. The laser pulses travel through these 550 ft cables to a pair of WCDs, where they are connected to a distribution box at the base of each pair of WCDs (see Figure 3.6).

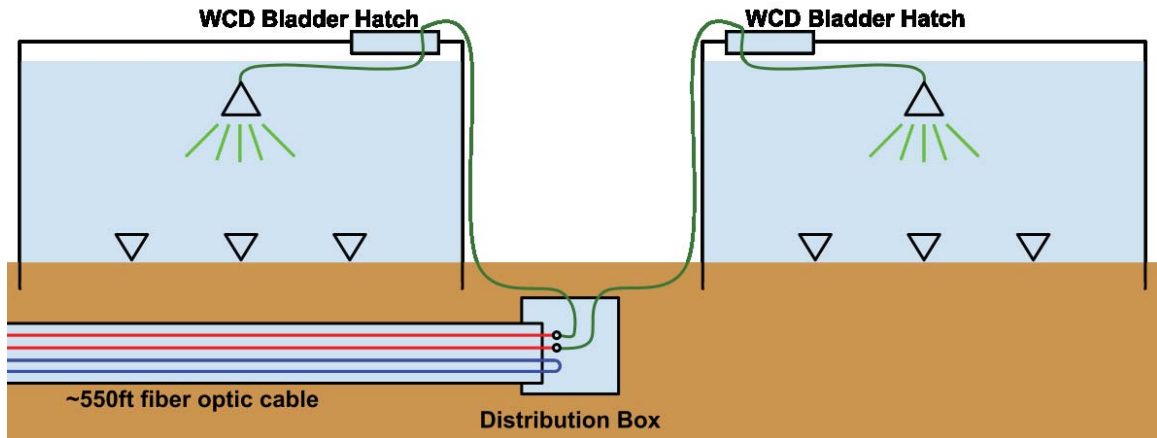


Figure 3.6: Diagram of the detector distribution box and connecting patch cables at each pair of detectors.

As can be seen in Figure 3.6, each length of fiber AB and CD is connected to a patch cable (the green lines in Figure 3.6) which runs through the WCD bladder hatch, and then connects to the floating diffuser, which is shown in Figure 3.7.

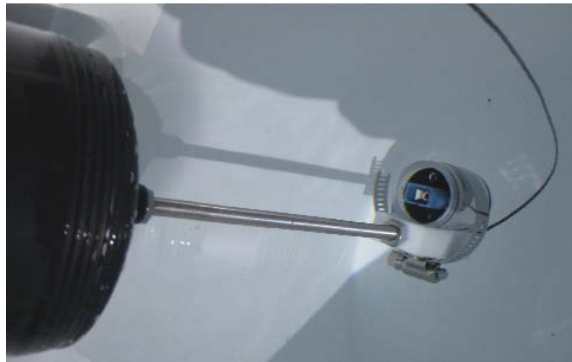


Figure 3.7: An image of the diffuser used in the WCDs.

3.1.4 RTT Network

The purpose of the RTT network is to measure the time it takes for a laser pulse to reach the detectors. This is done by routing two fibers out to each WCD with their ends connected in a loop, firing a laser pulse into one end, and timing how long it takes the pulse make the round trip. Dividing this time by two gives the time it takes the light to reach the WCD.

The reason for including this timing mechanism is to verify the behavior of the fiber-optic cables. One concern is that 500ft of fiber-optic cable will have a variation on the order of 0.1 ns in the transit time of the light pulse, and that this variation may be dependent on air temperature, ground temperature, or some other environmental effect.

The timing network starts with Splitter 1 in Figure 3.4, onto which the laser is directed. Splitter 1 is a 1:17 splitter, where one output fiber goes to Radiometer 1, and the remaining 16 output fibers are connected to Splitter Group 2 which consists of a set of 16x 1:10 splitters. One of the outputs of Splitter Group 2 is connected to a fast photodiode, which is used as the t_{start} timing signal, measured by a timing counter (see Appendix B.5). 150 more outputs from Splitter Group 2 are connected to the fiber E's in the 550ft cables as diagrammed in Figure 3.5. After the \sim 550ft cable, the output cable F's are then connected to Switch Group 2. As Switch Group 2 consists of two fiber-optic switches, they combine to make a 150:1 switch, which allows a single light path to be chosen, so that the round trip

time of one pair of WCDs can be measured at a time.

3.1.5 Interface with Data Acquisition System (DAQ)

The PMT data are recorded by the main DAQ system, and in order to assign calibration runs to these data, the calibration system and the main DAQ need to be synchronized. To properly identify calibration data within the DAQ, extra signals are sent to Experiment Control during a calibration run. Experiment Control (ExpCon) is the primary control program that manages all aspects of the observatory.

The first two signals involve the measurement of the round trip times. When the laser in Figure 3.4 is fired, Splitter Group 2 has one output fiber that is connected to a fast photodiode, Photodetector 1. This photodiode converts the photon pulse of the laser pulse in the fiber to a voltage pulse in a wire. This voltage pulse is discriminated and then directed into the main DAQ on a dedicated channel called t_{start} . When the calibration analysis is done, this t_{start} is used as a measure of when the laser is fired.

The second signal is similar to t_{start} , and called t_{stop} . This second signal is created by the return laser pulse, coming through Switch Group 2 and Splitter 3, then through Photodetector 2, then to a DAQ channel. The time that the laser pulse spent in the fiber can then be calculated by $(t_{start} - t_{stop})/2$.

The third signal (not pictured) is $t_{light_in_tank}$, and it is used as a notification to the DAQ that laser light is being sent to the PMTs. It is a μs -wide voltage pulse created by the same pulser device that triggers the laser.

3.1.6 Radiometer Usage

At four separate points the laser pulses' energies are measured with radiometers and probes from LaserProbe.com, models RM3700 and Rjp-465 (see Appendix B.8. The first measuring point is before the laser passes through the filter wheels, in Figure 3.4.

50% of the laser beam is split off with Beam Splitter 1 and directed onto the end of a fiber-optic splitter, where one fiber goes to Radiometer 1. The purpose of this radiometer is to keep track of the initial laser energy, before it is altered by the filter wheels.

Radiometer 2 is positioned after the filter wheels, utilizing the fiber-optic splitter that routes light to the Tanks. This radiometer measures the laser energy coming through 10 fibers from the initial splitter, recombining them with Splitter 4, and connecting the output to Radiometer 2. The purpose of this radiometer is to measure the transmission efficiency of a green filter combination.

Radiometer 3 is located further down on the fibers from the laser. The 10x switch modules within Switch Group 1 each have a set of outputs from 1-16, and fiber-optic cables going

to WCDs use ports 1-15. The 16th port on each switch module is connected to a backwards fiber-optic splitter (1:10), and the single output fiber is plugged into Radiometer 3. This radiometer allows for a measurement of the light being sent through each module in Switch Group 1. By turning all the modules in Switch Group 1 to their 0th “off” position, and setting one module to its 16th position, the transmission efficiency of that switch module can be measured.

Radiometer 4 is positioned just after the filter wheels, and takes a direct measurement of the laser beam, instead of measuring through a fiber. This increases the number of light intensities that can be measured by the radiometer, while an ND filter is used to keep from over-exposing the radiometer. The advantage of this technique is that some laser intensities are too low to be measured through a fiber, so this method moves them to a more appropriate range for the radiometer.

3.2 Control Software

The Calibration Control Software has been written to manage calibration runs and record calibration data. This software had to be custom made because the manufacturers do not provide drivers that can be used for continuous data acquisition and interfacing with other components as needed in an experiment like HAWC. The main method an operator controls the calibration system is through the CalUser program. This program sends short

commands through a terminal interface to the main calibration daemon, which is described in Section 3.2.1. Section 3.2.2 describes the use of sockets, and the various roles of each socket. Section 3.2.4 discusses the individual drivers that control the calibration hardware, and receive calibration data. Section 3.2.5 summarizes the two main tasks used by the calibration system in its general operation.

3.2.1 Daemon

The primary process is called the Calibration Daemon, or CalDaemon. It is a state machine, whose responsibilities include monitoring socket communications, managing the power for calibration hardware, and executing calibration Tasks.

The state machine has several different states, listed in Table 3.1, where each state has different behaviors, acceptable commands, and functions. The main states are ‘Idle’, ‘Running’, ‘Init’, and ‘Fault’.

The ‘Init’ state is used when the CalDaemon is first turned on, and is used to check that all the equipment is working. The majority of the time, the calibration system is in the ‘Idle’ state, where CalDaemon waits for an incoming command from either ExpCon or CalUser. When the ‘launch’ command is received, CalDaemon switches to the ‘Running’ state, during which it creates a thread which executes a calibration run. When a problem is detected in the ‘Init’ or ‘Running’ state, CalDaemon then shifts to the ‘Fault’ state, where

Table 3.1
Table of CalDaemon states

State	Purpose	User Commands	Connecting States
Init	Handle Startup	state? ls	Idle Fault
Idle	Wait for launch command	state? ls taskinfo launch diagnostic	Init Running Fault Diagnostic
Running	Currently executing a Task	state? ls taskinfo interrupt	Idle Fault
Fault	Error detected	state? ls diagnostic	Running Diagnostic
Diagnostic	Skilled Operator doing tests	state? ls taskinfo release, quicklaunch poweron poweroff	Idle,Fault
Diagnostic Running	Skilled operator executing a Task	state? interrupt, ls, taskinfo	Diagnostic

it sends an alert, and waits for a Calibration Expert to identify the problem.

3.2.2 Sockets

Sockets are the method used to send messages from one running program to another running program, either on the same computer or a different one. To handle sockets, the free ZMQ socket library is used[21]. This allows for the use of two kinds of sockets: a REQ-REP type socket[22], and a PUB-SUB type socket[23].

A REQ-REP type socket is a simple, one request, one reply socket. A single text string is sent out as the request, then it waits for a single response of a text string. By itself, this

allows for simple messages to be sent back and forth. With the addition of serialization, Python objects can be encoded to a single binary string, and can be sent back and forth over sockets. This allows for a simple integer or a complex dictionary to be sent over the socket.

A PUB-SUB type socket functions differently, where there can be one publisher (who has opened a PUB socket), and many subscribers (who have opened a SUB socket pointing to the PUB socket). The order which they are opened does not matter. This allows for the publishing of information to multiple programs, without having to change anything in the settings of the publisher.

One of the two primary roles of CalDaemon is to always be online and able to reply to requests. It keeps three REQ-REP sockets open, and one PUB-SUB socket open. All REQ-REP sockets are for incoming traffic (from ExpCon, CalUser, and TaskThread), and the PUB-SUB socket is for outgoing traffic to the ExpCon database.

The first socket is a REQ-REP socket, with the purpose of handling command messages from ExpCon. These messages are primarily for finding out what state CalDaemon is in, as well as starting and stopping calibration tasks. The messages exchanged here are JSON[24] serialized dictionaries.

The second socket is another REQ-REP socket, which communicates messages between CalDaemon and CalUser. Messages from CalUser are simple strings, containing a command, and several options. A calibration user can use the CalUser program to send

these messages to CalDaemon to change states, start a task, etc.

The third socket is a REQ-REP socket that listens for messages from a currently running task. When a task has recorded calibration data, it then sends it to CalDaemon via this REQ-REP socket. This is to make sure that any data (from CalDaemon or the task) sent to other places (ExpCon, other computers) comes from a single program, port, and socket. The data from the task is then forwarded to CalDaemon's PUB-SUB socket.

A fourth socket, a PUB-SUB socket, publishes data to ExpCon. This can be any kind of data, from CalDaemon state changes ("To ExpCon: CalDaemon is now in the Fault State"), to data recorded during a calibration subrun.

3.2.3 Interface with Experiment Control

In order to function in an automated fashion, CalDaemon must receive commands from another program running on another computer, called ExpCon. ExpCon sends commands to CalDaemon through one REQ-REP socket, and pushes out data through the PUB-SUB socket. Any communications with ExpCon are in the form of a command message, which consists of a date/time stamp, a service name (CalibrationService), a command word, and a dictionary of options. This is then serialized via JSON, and transmitted through the socket.

Data recorded by the calibration system is published to Expcon via a dictionary with several

pieces of information, which can be divided up into five groups.

The first group includes information identifying the calibration run:

- † RunYear, RunDay, RunSecond: date/time of the calibration run.
- † CalibRunID: calibration run identification number, given by ExpCon.
- † Version: version number.
- † CalibrationTaskFile: name of the calibration task.
- † CalibrationDataStage: stage of the calibration run.
 - A value of 1 indicates the start of a calibration run.
 - A value of 2 indicates the start of a calibration subrun.
 - A value of 3 indicates the end of a calibration subrun.
 - Full data is included in all CalibrationDataStage=3 messages.
 - A value of 4 indicates the end of a calibration run.

Another group involves information about the calibration subrun:

- † LaserFreq: The laser pulsing frequency.
- † WarmupTime: The duration of time the laser was fired for before starting the calibration run.
- † TankRegion: Set of detectors that light will is sent to.
- † NumberOfSubruns: Number of subruns in this calibration run.
- † SubrunID: ID of the subrun within a particular calibration run.

† TimeStart: Time when this subrun was started.

† TimeDuration: How long this subrun took.

The third group involves detailed information about the hardware configuration of the calibration equipment:

† FilterWheel1Position, FilterWheel2Position, FilterWheel3Position: position of filter wheels 1, 2, and 3.

† FilterWheelOptDep and FilterWheelOptDepErr: These are measurable quantities, used for storing the Optical Depth of the current filter wheel position, but are not primarily used or calculated by the calibration system, so these two data names are now vestigial. FilterWheelOptDep is α , the experimentally found optical depth of the filter wheel combination described by FilterWheel#Position. FilterWheelOptDepErr is the error on the measurement of FilterWheelOptDep. The optical depth α of a filter wheel position can be described by $I = I_0 \times 10^{-\alpha}$, where I is the Laser output intensity and I_0 is the open filter laser intensity.

† NumberOfLaserPulses: number of laser shots used in this subrun.

Each radiometer is also described by the following parameters:

† Rad1Range: range setting on Radiometer 1 for this subrun.

† Rad1Energy: mean energy recorded from Radiometer 1 for this subrun.

† Rad1EnergyError: “Error on the Mean” of Rad1Energy

- † Rad1NumberOfBadPulses: number of non-clean data values (non-clean energies are 0.0J or -1J) recorded by Radiometer 1 in this subrun.
- † Rad1GoodPulses: number of clean energy values (within valid energy range) recorded by radiometer 1.

The last group of data values contain timing data from the Universal Timing Counter, which measures the round trip time through an individual fiber loop. Their values are not filled in yet, as the Universal Timing Counter driver has not completely been tested at the time of writing. The parameters are:

- † RoundTripFiber: the timing loop fiber whose round trip time is measured.
- † RoundTripTime: mean measured round trip time of RoundTripFiber.
- † RoundTripTimeError: error on RoundTripTime.

3.2.4 Drivers

In order to control the large variety of equipment used in the calibration system, drivers are written using the scripting language Python[25]. Most involve basic commands that change settings on the equipment, or get the values of the settings from the equipment.

The simplest is the GP700 driver, which has two main functions, a SetOutputPort() and a GetOutputPort(). These alter the output port that the GP700 is routing light to. The

most complex is the RM3700 driver, which has to handle several different settings, as well as record laser pulse energies from the radiometer. In addition, the driver must handle “blocking”, where a function waits for a response from equipment, and does not let the program progress until there is a response. As there are multiple radiometers that need to record laser pulse energies, each radiometer must be managed by a separate sub-process, called a thread. Each thread independently sends commands to and receives data from a different radiometer. The RM3700 driver achieves this with a set of three functions: SingleShotArm(), SingleShotStart(), and SingleShotFinish(). SingleShotArm() sets up the thread (<1 sec), but does not start it. SingleShotStart() launches the thread, blocking for a very short amount of time (<1 sec). This thread can then run independently of the driver, allowing it to wait for energy measurements to be received from the radiometer. SingleShotFinish() can then be called, which will block until the thread completes or times out. By launching separate threads, multiple radiometers can be used singly or together in a simple interface, allowing for individual radiometers to be moved or removed quickly.

3.2.5 Tasks

Tasks are specially formatted Python scripts which CalDaemon can execute. They are defined by a single file, called a Task File, and are invoked by CalDaemon. This design is chosen for several reasons.

This design allows full use of the Python coding language. Python is a powerful language, providing much flexibility and ease-of-use that is required for long term implementation.

The Python language allows for the use of custom Python classes. The ControlCerebrate class has been written to control all the calibration equipment via high level functions. Alternately, the hardware drivers can be used instead, allowing for low-level control of each piece of equipment.

Since this design can run tasks in a separate thread, CalDaemon can always be available to receive and reply to REQ-REP sockets. Also, since CalDaemon is managing the tasks, it allows only one task to run at a time, preventing problems where two programs attempt to control one device.

Two tasks have already been written to accomplish the regular responsibilities that the calibration system must manage. The first task is the Radiometer Ranging Task, which calculates the best energy-range setting for each radiometer, filter wheel combination, and switch configuration. The process for calculating the best range is described below in Subsection 3.2.5.1. The second task is the Slewing Task, which executes a regular calibration run, and is detailed in Subsection 3.2.5.2.

3.2.5.1 Radiometer Ranging Task

The Radiometer Ranging Task decides on the best range setting of each radiometer, for each combination of filter wheels and switch settings. As the filters can adjust the laser intensity across seven orders of magnitude, and a single range setting on a radiometer only covers an energy range of three orders of magnitude (see Section 3.1), using only one range setting in each radiometer is not possible. Additionally, since the radiometers are at different positions in the setup (see Figure 3.4), their ranges need to be changed differently for different configurations.

By viewing Figure 3.4, it can be seen that while Radiometer 1 stays the same for all configurations, Radiometer 2 and Radiometer 4 need to change anytime the filter wheels rotate, and Radiometer 3 changes anytime the filter wheels or fiber-optic switches change. A rough estimate shows that with 100 filter wheel settings and 10 different fiber-optic switch modules, there are 1000 different configurations that each need separate radiometer range settings. Firing the laser for each of the more than 1000 configurations is an ideal job for a computer, thus the Radiometer Ranging Task has been written to carry out these measurements and find the best radiometer ranges for all configurations. Also, during the development of the calibration system, hardware was frequently repositioned for each different systematic studies, meaning the radiometer ranges would become out-of-date. This task could then be used to quickly find the best radiometer ranges for any particular

setup of the calibration system.

The process of finding the best radiometer range requires the following steps:

1. Set filter wheels and switch modules to one configuration.
2. Fire 1000 laser shots at 250Hz, and record the energies at each range setting.
3. Check that 95% of all 1000 laser shots were detected. Any lower than 95% means the energies are at or beyond the edge of the current ranges limits.
4. Check that the mean energy of the 1000 laser shots is at least $2 \times (\text{std-of-the-mean})$ away from the minimum energy and the maximum energy for that range.
5. Check that relative error (std/mean) for each 1000 laser shots is < 0.1 .
6. For each filter wheel, fiber-optic switch, and radiometer, the lowest energy range is chosen because it has a better energy resolution.

The best settings found by this procedure are saved to a settings file, which is then used later by the ControlCerebrate class.

3.2.5.2 Slewing Task

The purpose of the calibration system is to record the slewing time, or PMT response time, for each PMT at multiple light intensities.

The slewing task is a list of instructions that cycle through all filter wheel combinations,

fire laser pulses, and route light to the PMTs with the fiber-optic networks. Upon arrival at the PMTs, the laser pulses create between 0.1 and 10,000 PE signals. The multi-PE signal travels through the data cable to the electronics, where it is digitized into binary data.

The PMT response time is then calculated in the following method. t_{start} is the signal the calibration system sends to the DAQ to record when the laser is fired. t_{digit} is the time at which the first signal from a PMT is digitized.

1. The calibration system measures the time between when the laser is fired, t_{start} , and the time that the signal from the PMT is digitized, t_{digit} . The time difference between these two is equal to the times the laser and signal each spent in fiber, water and cable. $t_{start} - t_{digit} = t_{fiber} + t_{water} + t_{cable}$
2. The PMT response time is t_{cable} , which can be solved for. t_{fiber} can be measured with the RTT network, and t_{water} can be calculated, yielding the equation $t_{cable} = t_{start} - t_{digit} - t_{fiber} - t_{water}$
3. Each laser shot now has a t_{cable} for each laser pulse, which can be compared to the Time Over Threshold (TOT) of the laser pulse.

In Figure 3.8, the TOT and t_{cable} data is shown. This plot of TOT vs t_{cable} is called a slewing curve, and consists of data from the HAWC test WCD at Colorado State University.

In the figure, the red curve is found by using $t_{digit_low_thresh}$ and LowTOT. $t_{digit_low_thresh}$ is the time when the laser signal is digitized by the low threshold and LowTOT is the time

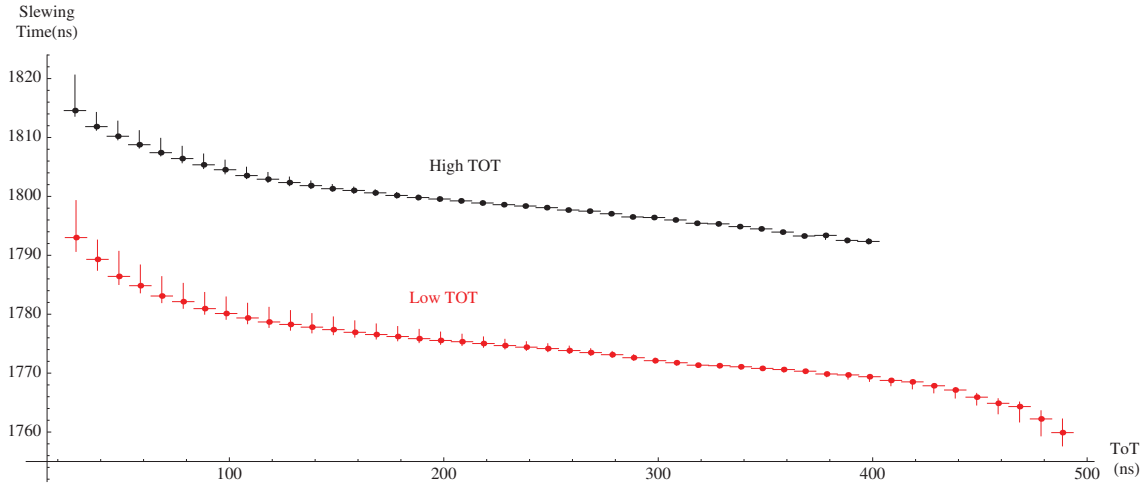


Figure 3.8: Slewing Curve: t_{cable} vs TOT.

duration the signal over the low threshold. The low threshold is set to a voltage equivalent to 0.5 PEs. The black curve is found similarly, using $t_{digit_high_thresh}$ and HighTOT, which both use a high voltage threshold equivalent to 4 PEs. The slewing times are inversely proportional to the TOT, because when a high-intensity light pulse strikes the PMT, there are more photons, with a higher probability that one of the photons arrives earlier. The slewing curves are different for each PMT, due to minute differences in the construction and electronics used for different PMTs.

This slewing curve is the first set of information that is provided to the reconstruction group, which is tasked with reconstructing the full shower. The second set of information is called the TOT-to-PE conversion, which translates each different TOT into an equivalent number of PEs. The number of PEs is important, in that it allows the HAWC observatory to assign a quantity of charge to each PMT that detects a shower. This determines how intensely each PMT is hit, and thus how far from the shower core the WCD is.

This TOT-to-PE conversion is found by looking at PMT data with the lowest light intensities, where each laser pulse does not have enough photons to strike the PMT with 100% of laser pulses in a set. By examining the fraction of laser pulses that were detected divided by the number of laser pulses fired, the occupancy $\eta = \frac{N_{hit}}{N_{fired}}$ can be calculated for each filter wheel position, after several thousand laser pulses. Through this method (called the occupancy method, described in [26]), the mean number of PEs at each occupancy level can be found. The mean PEs at other 100% occupancies can then be found by taking the ratios of filter wheel optical densities. This produces a TOT-PE curve, which is the set of information that is passed to the reconstruction group.

By performing slewing task calibration runs, the slewing curve and the TOT-PE curve can be found for each PMT. These curves are used to reproduce, for a given TOT, the time that a group of photons strike the PMT, and the number of photons in that signal. This information is then used by the reconstruction group to improve the accuracy of shower reconstructions.

Chapter 4

Systematic Studies

Systematic studies were performed to test the stability of the calibration hardware. The purpose of these studies is to verify that the system performance over long periods of time (days) is stable and repeatable. This is required, because one of the responsibilities of the calibration system is to monitor the stability of the experiment independently of systematic variations of the calibration system itself. Since the conversion of Time Over Threshold (TOT) to PhotoElectrons (PEs) requires use of the occupancy method (see Subsection 3.2.5.2), the laser is required to be stable within 5%.

For this chapter, a “set” refers to a group of laser pulses fired in succession at the same pulsing frequency, and with the same filter wheel, switch, and radiometer settings.

4.1 Pulsing Frequency

The first equipment to be tested is the laser, examining the time dependence of the pulse energy. As the calibration system needs to be stable over time, this property is critical.

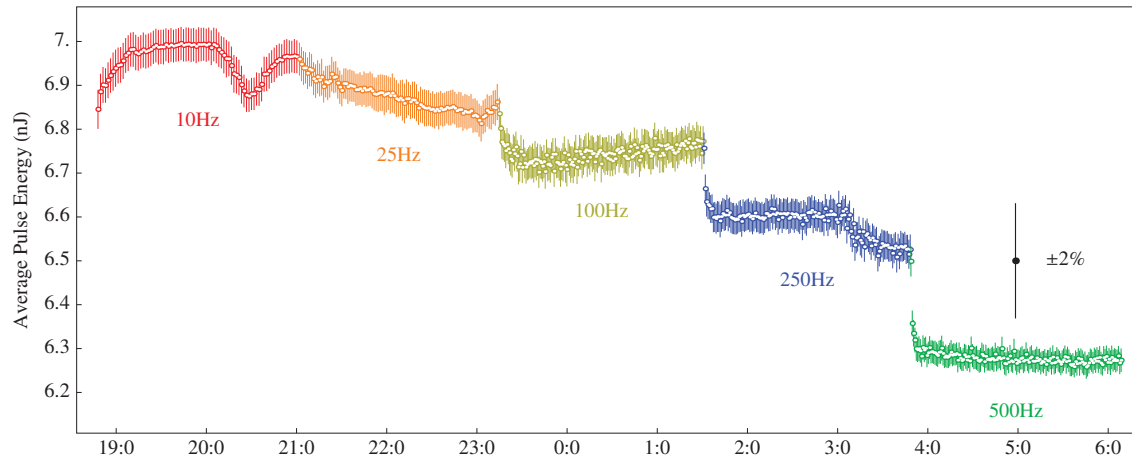


Figure 4.1: Laser Pulse Energy as a function of time and pulsing frequency.

Figure 4.1 shows the laser pulse frequency as a function of time and pulsing frequency. The laser is pulsed for 160 minutes at five different pulsing frequencies: 10Hz, 25 Hz, 100Hz, 250Hz, and 500Hz. Each point represents one set of 1000 laser pulses, with their mean and ± 1 standard deviation. It can be seen that at each pulsing frequency, the mean energy of each set of pulses decreases as the pulsing frequency increases.

When the pulsing frequency is changed, the first ~ 2000 pulses are higher energy than the rest of the pulses at that frequency. This implies that when using a new pulsing frequency, a warm-up time of around 30 to 45 minutes is needed to allow the laser to reach equilibrium

at the beginning of a calibration run.

In a followup experiment where the pulsing frequency is randomized, it is found that the pulse energy is also slow to rise to its equilibrium energy, as seen in Figure 4.2. Since the laser is slow to both rise and fall to its equilibrium energy, this can be viewed as the laser reaching thermal equilibrium. The warm-up period will be taken into account in the analysis of calibration data.

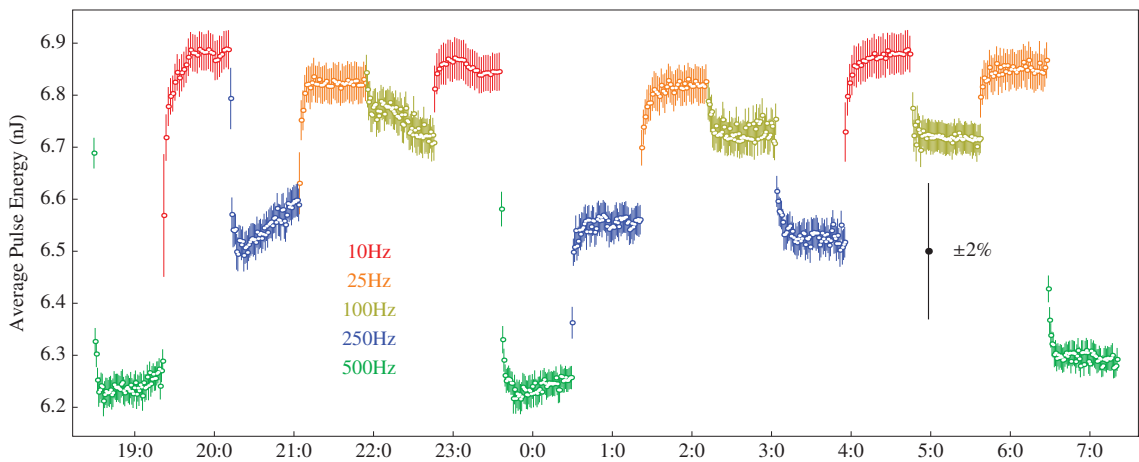


Figure 4.2: Laser sets using different pulsing frequencies.

Another feature which may affect the calibration analysis is that there are changes in the average pulse energy. Namely, in the 10Hz and 250Hz sections, variations on the order of two standard deviations (around 2%) can be seen. When implemented in the HAWC experiment, the laser will pulse at two predefined frequencies, at 250 or 500Hz (fast mode) or 10Hz (slow mode). These variations are within the requirement that the laser energy is allowed to drift (within 5% for those predefined frequencies).

4.2 Radiometer Triggering Modes

A separate experiment is done to examine the performance of the radiometer in different radiometer trigger modes. The RM3700 radiometers (see Appendix B.8) have three different trigger modes:

1. Automatic internal triggering. When the pulse energy rises above 10% of the minimum energy of the current range setting, the radiometer starts integrating.
2. External Triggering, positive slope. A trigger pulse is generated by the pulser, and the radiometer triggers on the rising edge of that trigger pulse.
3. External Triggering, negative slope. A trigger pulse is generated by the pulser, and the radiometer triggers on the falling edge of that trigger pulse.

Figure 4.3 shows energy measurements taken with the three different trigger modes. As can be seen when the internal triggering is used, one set out of every 20 or 30 has an abnormal standard deviation. An examination of these errant sets, one of which is plotted in Figure 4.4, shows that the internal triggering sometimes does not measure the first pulse in a set correctly. The radiometer measures the first pulse (marked by an arrow) at a much lower energy than the rest of the set, which increases the standard deviation of the set.

As a result of this study it was decided to externally trigger the radiometers in the HAWC calibration system.

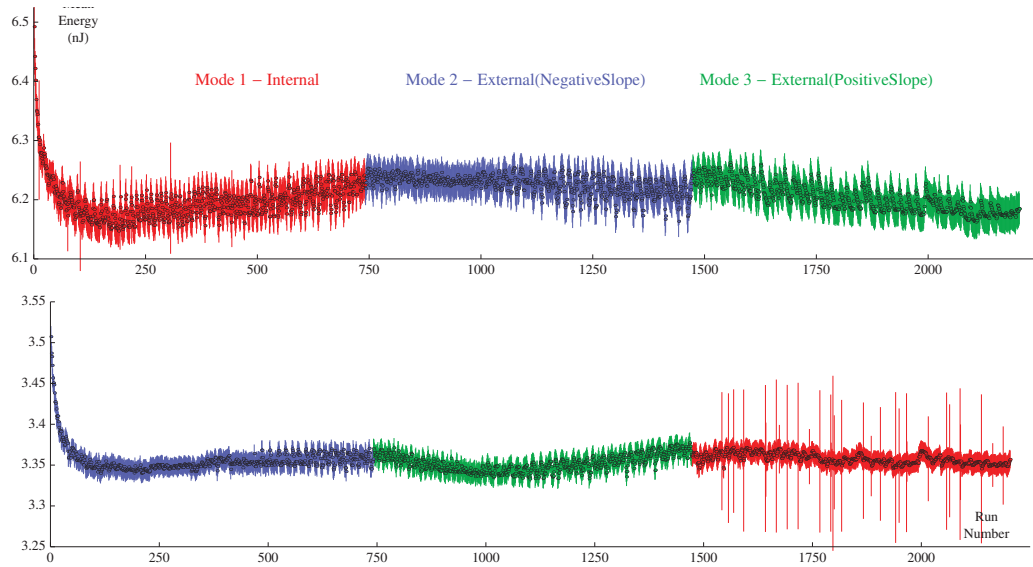


Figure 4.3: Laser energy measurements of the radiometers in three different triggering modes.

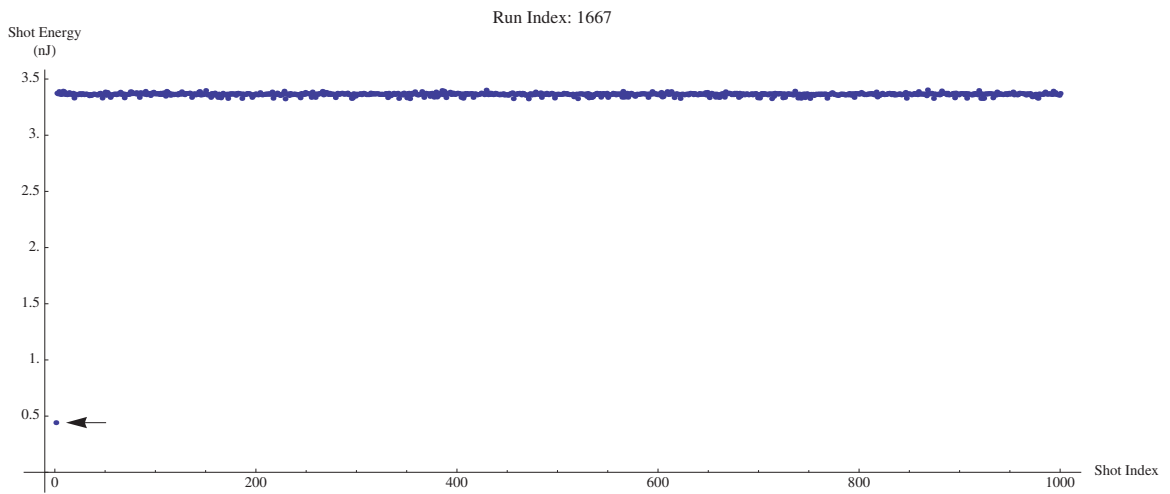


Figure 4.4: Individual laser pulse measurements from a radiometer using internal triggering. The first incorrect measurement is marked by an arrow.

4.3 Filter Wheel Repeatability

The calibration system will be run on a regular basis, performing calibration runs on a weekly or monthly basis. These runs will require rotating the filter wheels through many positions, so it is important to test how well the filter wheels return to specified positions over many rotations. A feature of the filter wheels automatically realigns them to an absolute position every time they are restarted[19], but since they are not restarted during a calibration run, the long-term drift is examined. To test the long-term drift of the filter wheels, a study is performed where multiple filter wheel combinations were used over a long period of time.

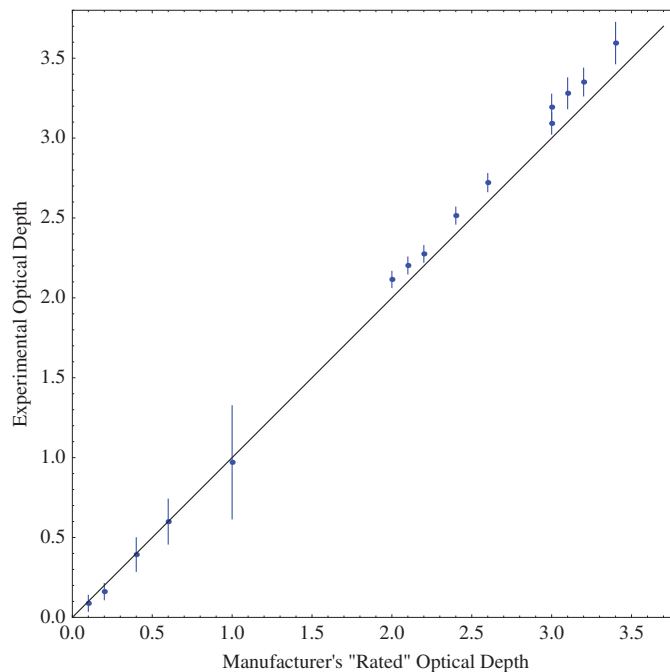


Figure 4.5: Manufacturer Rated Optical Density vs Experimental Optical Density. The black line is $x=y$ line for perfectly behaving filters.

The experiment rotated through all 36 filter wheel combinations for two filter wheels 180 times each, over a period of eight hours. No significant deviations in the measurement of transmission efficiencies were found. As part of the study, the optical density of each filter wheel combination is calculated experimentally using the radiometer measurements and compared to the “rated” optical density from the manufacturer. The results are shown in Figure 4.5. The differences are due to the wavelength dependence of the transmission efficiency of the filters, as shown in Figure 4.6. In these figures it can be seen that the “rated” filter transmission efficiency is more accurately described as “the average transmission efficiency for wavelengths between 400 nm and 700 nm.” As the transmission efficiency is higher at 700 nm, this will increase the average transmission efficiency across this range. Examining the filters with higher optical depths (the middle and right plots in Figure 4.6), the ratio of the transmission efficiencies at 700 nm and 532 nm is larger than in the low optical depth filters (the left plot in Figure 4.6). After converting the transmission efficiencies to optical densities, these different ratios explain why the filters with a “rated” optical depth greater than 1.5 are all found to have a higher experimental optical density, while lower “rated” optical density filters are closer to their experimentally found optical densities.

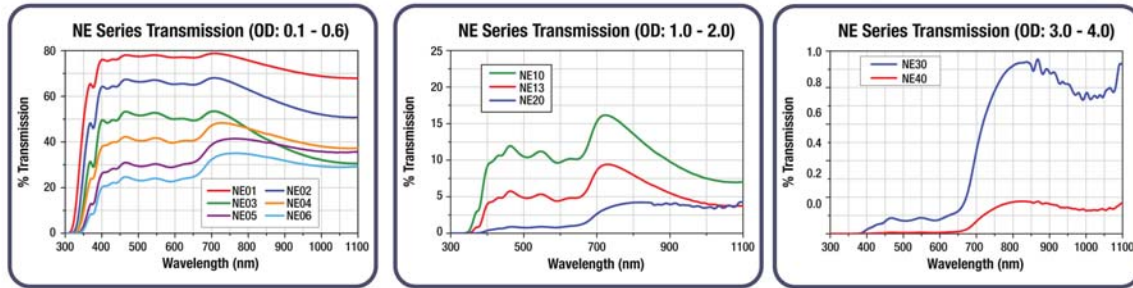


Figure 4.6: Transmission efficiencies for the Thorlabs NE series filters used in the filter wheels.[27]

4.4 Temperature Dependence

In Section 4.1, it is found that the laser must reach thermal equilibrium, and a follow-up study is done to investigate how the ambient temperature affects the laser output energy.

In the study, the laser is fired at 100Hz for several hours while the temperature is recorded with a thermometer located on the same table as the laser.

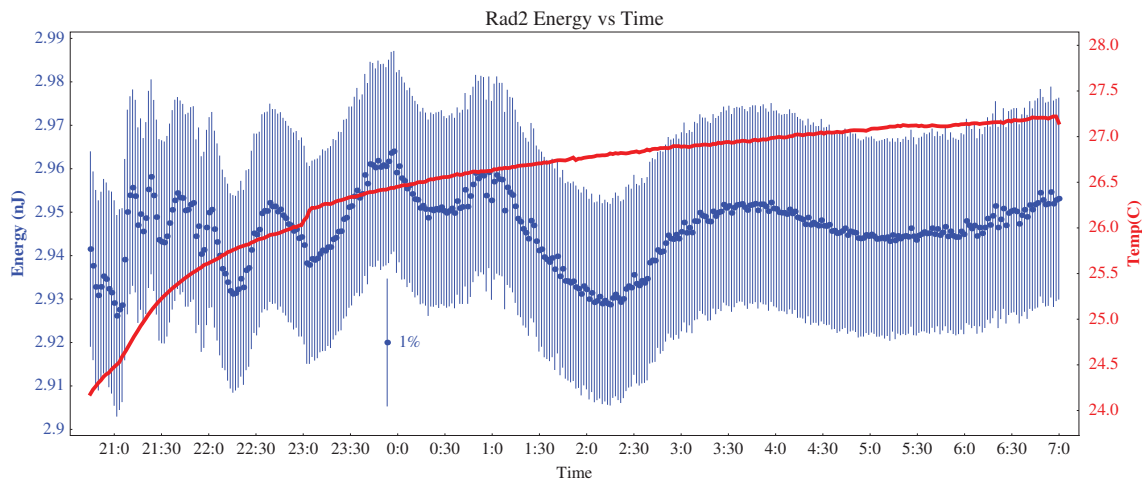


Figure 4.7: Laser Energy and Room Temperature vs Time. Mean pulse energy is shown in blue, with 10,000 pulses per point. Room temperature is shown in red.

As can be seen in Figure 4.7, the measured temperature changes over 3°C , while the pulse energy varies by 1%. No direct correlation between temperature and pulse energy is detected.

A second-order effect can be noted between the slope of the temperature and the oscillation frequency of the energy. In the first three hours of data, the energy oscillation frequency is high, and the slope of the temperature is large, but in the last four hours, the oscillation frequency and slope of the temperature are both low. This effect may be due to the structure of the beam changing on scales similar to the size of the core of the fiber-optic cable, which is discussed in Section 4.5.

4.5 Multifiber Testing

The calibration system utilizes several fiber-optic splitters and switches to route light through the PMT and RTT networks. To launch laser pulses into the networks, the pulses are directed onto the ends of two fiber-optic splitters, (see Figure 3.5, Splitters 1 and 3).

As the fiber takes only a small fraction of the energy of the full beam, it is important to measure the energy output of different fibers in a splitter, and study if they are stable with time. If they are not stable with time, the radiometers will record energies that are not representative of the light intensity being sent to the WCDs.

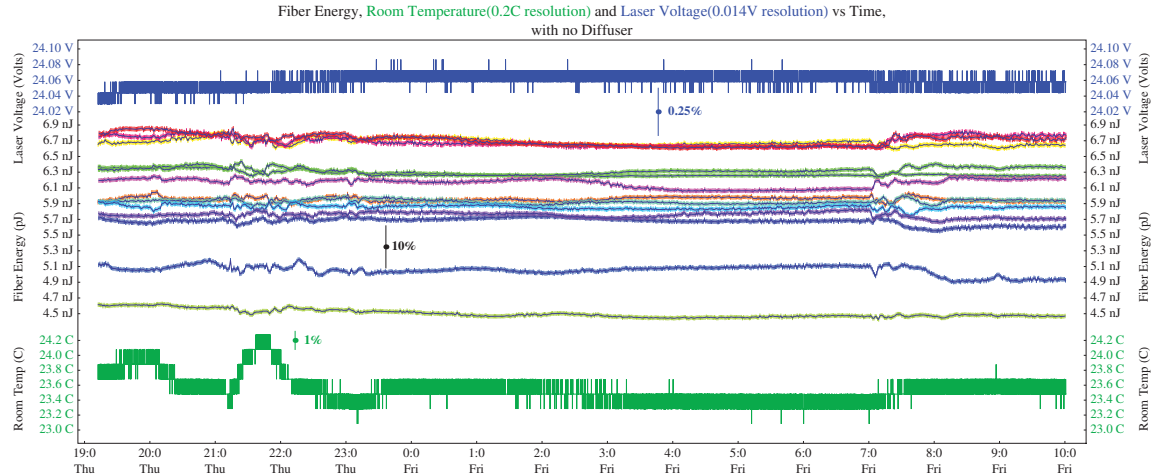


Figure 4.8: Laser Energy, Laser Voltage, and Room Temperature with respect to time. Blue at the top is laser input voltage, green at the bottom is room temperature, thinner lines in the middle are average energy recorded via each fiber of a 1:37 splitter.

The fiber-optic switch is used to cycle through the different output fibers of the 1:37 splitter that will be used in the HAWC experiment (see Splitter 3 in Figure 3.5) The data from this study is shown in Figure 4.8. The multi-colored thin lines in the center represent the measured energies for individual fibers.

The mean energy in each fiber is constant (within 3%), but varied from fiber to fiber by as much as 30%. It is important to note that this 30% is a combination of the splitter efficiencies and the GP750 switch efficiencies, both of which are different for each fiber/switch output path. This is acceptable because the acceptable variation on the energy is 5%.

Figure 4.8 also shows the measured voltage of the laser power supply (top blue line) and the room temperature (green bottom line).

No effect of the variations in laser voltage on the output energy is discernible. The changing temperature on the other hand causes fluctuations in the individual fiber energies. The energy in some fibers increases while the energy in others decreases. This can be interpreted as a sign that the total pulse energy is not increasing or decreasing, but that the laser pulse structure is changing a size scale similar to size of the fiber-optic cores, $125\ \mu\text{m}$ (diameter).

To confirm this interpretation, a CCD is used to take pictures of individual laser pulses. One of these images is shown in Figure 4.9. The size of a single fiber-optic cable and the fibers

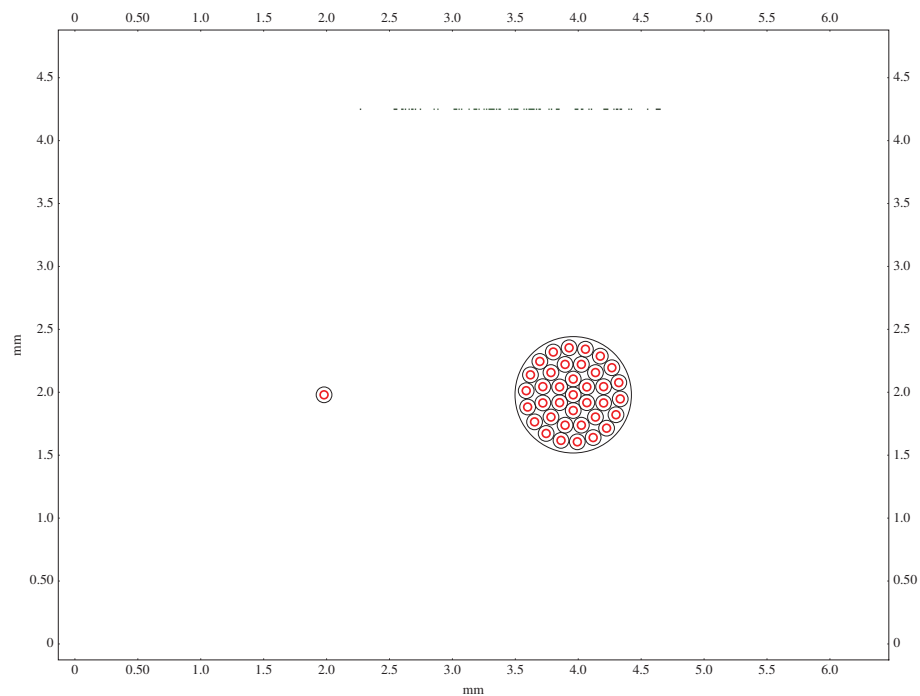


Figure 4.9: CCD profile of the laser beam, with a single fiber and bundle splitter for reference. The black circles denote the cladding of the fiber, and the red circles denote the cores. The large diffraction pattern is mostly likely due to the filter wheels.

of a splitter are shown to scale. The black rings indicate the outer boundary of the cladding,

and the red rings indicate the outer boundary of the core of the fibers. The distance from maximum to maximum in the pattern is of a similar scale as the fiber-optic core diameter.

In a series of several images of laser pulses taken over time, it is noted that the diffraction pattern drifted several hundred μm in one direction over the course of several minutes of laser shots, supporting the explanation given above.

To attempt to reduce and smooth the differences and variations between different fibers in the splitters, a diffuser (made of a 2 mm thick disk of virgin teflon) is placed 3 cm up-beam from the splitters. The previous study is then repeated, and the data is shown in Figure 4.10.

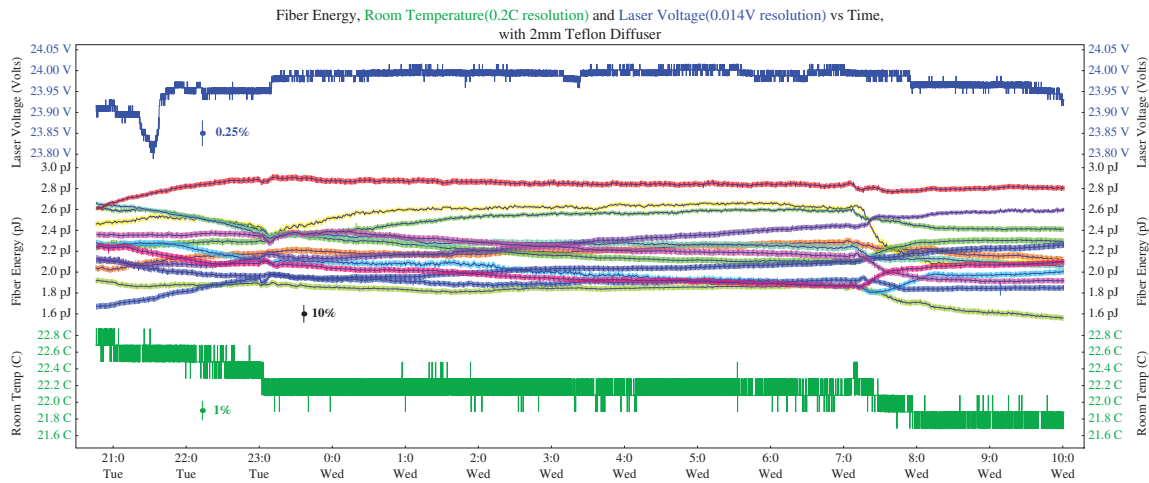


Figure 4.10: Laser Energy, Laser Voltage, and Room Temperature with respect to time, using a diffuser in the laser setup. Blue at the top is laser input voltage, green at the bottom is room temperature, thinner lines in the middle are average energy recorded via each fiber of a 1:37 splitter.

It can be seen that the fibers now vary in time by as much as 20%, which reduces the stability of the calibration system. In addition, the fiber energies are reduced by

approximately three orders of magnitude. For these reasons this diffuser is not used in the final design of the calibration system.

4.6 Radiometer Range Determination

The goal of sending 0.1 to 10,000PEs to the PMT requires the radiometers to be able to measure light pulses across five orders of magnitude. It is found that the radiometer can record energy measurements below energy ranges stated by the manufacturer. In order to find the true low-energy limit of the radiometers, the following study is performed. Two radiometers record laser pulse energies simultaneously, one through a fiber, the other by direct exposure to the beam. The data from this study is shown in Figure 4.11.

The top group of energies are measurements of half of a laser pulse, recorded using a radiometer that measures the full beam (circles).

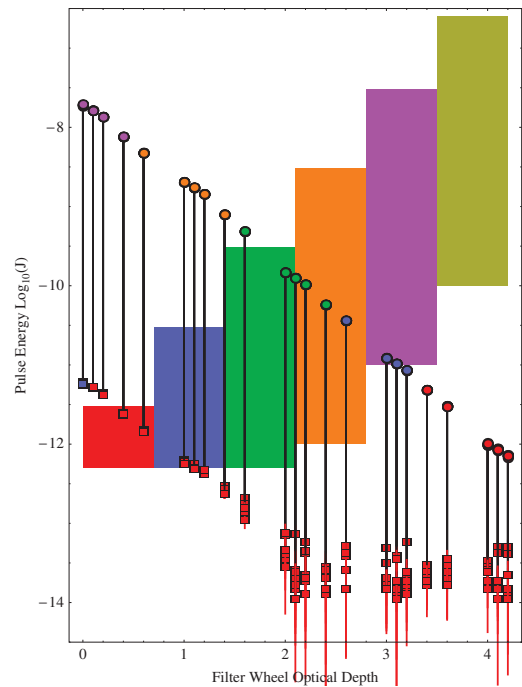


Figure 4.11: Filter Wheel Optical Depth vs Measured Pulse Energy. The color rectangles in the background show the six radiometer energy ranges, and the color of the points shows the energy range that they were recorded with. The black lines connect measurements taken at the same filter wheel combination.

The bottom group of energies are measurements of the other half of each pulse, recorded using a radiometer that measures the pulses through a fiber (squares). This provides a “true” radiometer energy in the top group, and an “extended range” radiometer energy in the bottom group. As the fiber core area is three orders of magnitude smaller than the beam area, the energies are similarly reduced in the figure. Both groups are linear from an optical density 0.0 to 1.9, but beyond 1.9, they are no longer both linear. The energies through the filters are too small for the radiometer to measure.

Two sets of pulses measured through the filter near this sensitivity boundary are examined in figure 4.12. In the top plot, a histogram of a set of 2000 laser pulses is shown, using a filter wheel with an optical depth of 2.0, and a gaussian is fitted to the histogram. The bottom plot is the same, except a filter wheel optical density of 2.2 is used. From the figure, it can be seen that the mean energy is less for the higher optical density filter. Additionally, the bottom histogram is partially cut off, indicating a hard limit in the digitization of the energy measurements. To accurately calculate the mean energy for a set of laser pulses, a gaussian fit is performed and the fitted mean (+error) is used as the energy value. The peak of the gaussian must be above $3.5 \times 10^{-14} \text{J}$ to be counted as a valid measurement.

This limit is implemented in the Radiometer Ranging Task as the minimum energy for the lowest energy range, meaning the calibration system will not attempt to use filter wheel combinations that reduce the laser energy measured at each radiometer below this minimum energy.

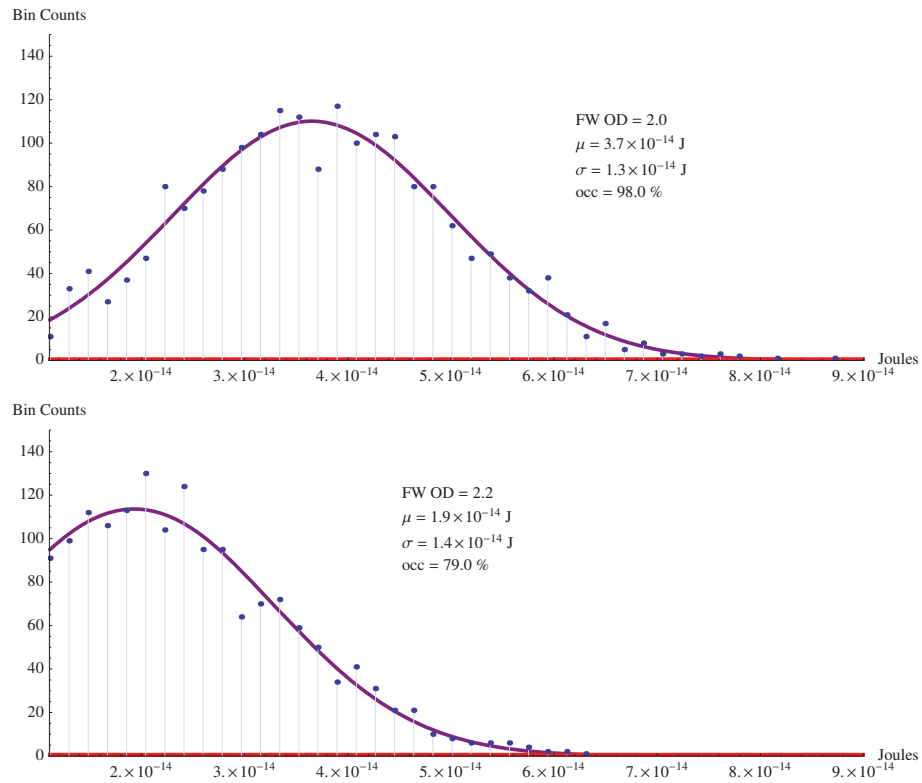


Figure 4.12: Laser Energy Histogram. The top plot is a histogram of 2000 laser pulse energy measurements using a filter wheel optical depth of 2.0. The bottom plot is a histogram of 2000 laser pulse measurements using a filter wheel optical depth of 2.2.

Chapter 5

Conclusion

The HAWC calibration system, consisting of a laser system and two fiber optic networks, has been tested at Michigan Technological University and at Colorado State University. This calibration system is capable of delivering from 0.1 PEs to 10,000 PEs, to all PMTs in HAWC. The system and its component parts have been shown to operate stably, possessing a variation in laser pulse energy of less than 5%. The beam structure has been studied, and has been found to change over the course of minutes. This does not significantly impact the variation of the laser pulse energy that is output by the fibers.

A control software package to manage the calibration system has been developed. This includes the human interaction program CalUser, a background process called CalDaemon to manage commands and calibration runs, a task system for scriptable calibration runs,

and a set of equipment drivers to control calibration devices. The interface between CalDaemon and the software that controls the entire HAWC experiment (“Experiment Control”, or ExpCon) has been tested at University of Wisconsin-Madison. This interface allows CalDaemon to receive commands to start and stop calibration runs, report the state of the calibration subsystem, and send calibration data to experiment control.

Future studies for the calibration system performance include the effects of using an optical-quality 1500-grit diffuser, placed less than 1 cm from the end of the fiber optic splitter. Additionally, a timing unit must be implemented into the system to measure the time the laser pulse spends in the fiber.

In the fall of this year, the MTU laser system will be moved to the HAWC site in Mexico. It will first be tested independently with a subset 30 Water Cherenkov detectors (i.e. 120 PMTs). Once the HAWC experiment is fully operational, experiment and calibration control will run together in an automated mode, performing periodic calibration runs while cosmic ray data is taken.

References

- [1] J Blümer, et al, “Cosmic Rays from the Knee to the Highest Energies,” *Progress in Particle and Nuclear Physics*, vol. 63, no. 2, pp. 293 – 338, 2009.
- [2] W Atwood, et al, “The Large Area Telescope on the FERMI Gamma-Ray Space Telescope Mission,” *The Astrophysical Journal*, vol. 697, pp. 1071–1102, 2009. doi:10.1088/0004-637X/697/2/1071.
- [3] F Aharonian, J Buckley, T Kifune and G Sinnis, “High Energy Astrophysics with Ground-based Gamma Ray Detectors,” *Rep. Prog. Phys.*, vol. 71, 2008.
- [4] E Aliu, et al, “Detection of Pulsed Gamma Rays Above 100 GeV from the Crab Pulsar,” *Science*, vol. 334, no. 6052, pp. 69–72, 2011.
- [5] J Holder, et al, “The First VERITAS Telescope,” *Astroparticle Physics*, vol. 25, no. 6, pp. 391 – 401, 2006.
- [6] F Aharonian, et al, “Calibration of Cameras of the H.E.S.S. Detector,” *Nuclear Instruments and Methods in Physics Research A*, vol. 22, Issue 2, pp. 109–125, 2004.

- [7] D Ferenc, “The MAGIC Gamma-ray Observatory,” *Nuclear Instruments and Methods in Physics Research A*, vol. 553, pp. 274–281, 2005.
- [8] T C Weekes, et al, “Observation of TeV Gamma Rays from the Crab Nebula using the Atmospheric Cerenkov Imaging Technique,” *The Astrophysical Journal*, vol. 342, pp. 379–395, 1988.
- [9] R Atkins, et al, “Observation of TeV Gamma Rays from the Crab Nebula with Milagro Using a New Background Rejection Technique,” *The Astrophysical Journal*, vol. 595, pp. 803–811, 2003.
- [10] J Ahrens, et al, “Sensitivity of the IceCube Detector to Astrophysical Sources of High Energy Muon Neutrinos,” *Astroparticle Physics*, vol. 20, no. 5, pp. 507 – 532, 2004.
- [11] W Apel, et al, “The KASCADE-Grande Experiment,” *Nuclear Instruments and Methods in Physics Research A*, vol. 620, pp. 202–216, 2010.
- [12] O Gress, et al, “The Study of Primary Cosmic Rays Energy Spectrum and Mass Composition in the Energy Range 0.5 - 50 PeV with TUNKA EAS Cherenkov Array,” *Nuclear Physics B (proc. Suppl.)*, vol. 75A, pp. 299–301, 1999.
- [13] Hamamatsu, *Hamamatsu R5912 PMT*, 2012. http://sales.hamamatsu.com/assets/pdf/parts_R/LARGE_AREA_PMT_TPMH1286E05.pdf.
- [14] Hamamatsu, *Hamamatsu R7081 PMT*, 2012. http://sales.hamamatsu.com/assets/pdf/parts_R/LARGE_AREA_PMT_TPMH1286E05.pdf.

- [15] The HAWC Collaboration, “Construction of the HAWC Gamma-Ray Observatory,” 2011. http://hawc.umd.edu/internal/db/2087_01.pdf.
- [16] CAEN, *VX1190A/B Technical Information Manual*, 2012. <http://www.caen.it/csite/CaenProd.jsp?idmod=786&parent=11>.
- [17] E. Hays, *A Search for TeV Emission from Active Galaxies*. PhD thesis, 2004.
- [18] T. Photonics, *PNG Lasers by Teem Photonics*, 2012. www.teemphotonics.com.
- [19] S. Products, *Spectral Products AB301-T Filter Wheel*, 2012. www.spectralproducts.com.
- [20] P Huentemeyer, et al, “Calibration of the HAWC Observatory,” in *International Cosmic Ray Conference*, HAWC Collaboration, 2011.
- [21] “The Intelligent Transport Layer - zeromq,” 2012. www.zeromq.org.
- [22] “ZMQ, The Guide - Ask and Ye Shall Receive,” 2012. <http://zguide.zeromq.org/page:all#Ask-and-Ye-Shall-Receive>.
- [23] “ZMQ, The Guide - Getting the Message Out,” 2012. <http://zguide.zeromq.org/page:all#Getting-the-Message-Out>.
- [24] “JSON,” 2012. www.json.org.
- [25] “Python Website,” 2012. www.python.org.

- [26] L Fleysher, R Fleysher, T Hains, “Methods of Photo-Electron Calibration,” *Milagro Internal Tech Note*, 2000.
- [27] Thorlabs.com, *Absorptive Neutral Density Filters: 400-700nm*, 2012. <http://www.thorlabs.com/catalogpages/V21/828.PDF>.
- [28] H Voelk, K Bernloehr, “Imaging Very High Energy Gamma-Ray Telescopes,” *Experimental Astronomy*, vol. 25, pp. 173–191, 2009.

Appendix A

Software

Socket

A means for one program to send simple messages to another program.

Thread

A means for a program to run several lists of commands at the same time

Blocking

When a function deliberately waits, either due to waiting for a hardware response, or due to a `time.sleep()` used in the code.

Port

A number assigned to a socket, which the computer uses to determine where socket traffic is routed to. (Web page calls use port 80, ssh uses port 22, CalDaemon ports are located in `$CAL/Settings/SocketSettings`).

Task

A specially formatted python script, which CalDaemon can execute via the launch command. All tasks are located in \$CAL/Tasks .

ExpCon

Short for Experiment Control, the main computer that controls the HAWC experiment. CalDaemon takes orders from this “boss” computer and reports to it.

Appendix B

Calibration Hardware

B.1 Laser

The laser is a PowerChip laser (<http://www.teemphotonics.com/>), capable of producing laser pulses with an average energy of 45 uJ per pulse, at a rate of up to 500Hz. This allows for each calibration run to only last several seconds, but gather several thousand measurements. The laser is ideally triggered on the positive edge of a squarewave voltage pulse, with a width 55 μ s and a height of 4.5V above ground.

B.2 Laser Power Supply

The laser power supply is an Acopian model A24H850M power supply. It provides DC power to the laser at 24 V, up to a maximum of 8 Amps. Its voltage is measured by the LabJack U3 DAQ board, through a small voltage divider.

B.3 Filter Wheel

There are three filter wheels used in the setup. They are model AB301-T filter wheels from www.spectralproducts.com. Each filter wheel has slots for six 25 mm diameter filters. Each slot is filled with either a NE_(optical density)_B filter from Thorlabs.com (see table B.1), or a thick piece of cardboard for an opaque slot, or left empty as an open slot. Each filter wheel communicates with the calibration control computer via a USB-serial cable and the PySerial python module. The list of filters and their optical depths is as follows:

Pos	FW1	FW2	FW3
1	Opaque	Open	Opaque
2	Open	0.2	Open
3	1.0	0.4	0.3
4	2.0	0.6	1.0
5	3.0	0.8	1.3
6	4.0	1.0	2.0

Table B.1
Optical Depth of Filter Wheel Filters

B.4 Pulser

The pulser is a Berkeley Nucleonics Model 575 Pulse/Delay Generator. Used to trigger the laser, by sending square-wave pulses (between 10 and 500/second) with a width of $55\mu\text{s}$ and a amplitude of 4.5V above ground. The device communicates with the calibration control computer via a USB-serial cable and the pyserial python module. The pulser also creates a signal for the TDC's. Any time light is sent into the tanks, an accompanying signal from the pulser is sent to the TDCs, indicating that light may be in the tanks. As light can be routed from 2 to 20 tanks at a time, a calibration run also requires notifying which tanks are having light routed to them.

B.5 Timing Counter

The timing counter is a Berkeley Nucleonics BN1105 timing counter. It cannot report a timing measurement at 500Hz. Initial tests point to it working as fast as 10Hz, so a separate thread will be needed to measure the timing fibers.

B.6 Fiber Optic Switch

To route the light to each tank, several fiber optic switches are used. The Dicon company's model GP700 and GP750 are the two switches used. Each GP750 switch (SW1 and SW2) have a bank of switch modules. SW1 will have 5x switch modules, and SW2 has 5x switch modules. Each switch module has 1 input, and 16 outputs, and a 17th output that serves to block the light. Based on this design of the PMT Fiber Optic Network, we can route light to 2, 4, 6, 8, 10, 12, 14, 16, 18, or 20 tanks at a time.

B.7 Milagro Fiber Optic Switch

A Dicon GP700 fiber optic switch, with 1 input, 64 outputs, and 1 off position. It is found that the switch's efficiency with the green laser is around 3%, most likely due to the reflective coatings inside the switch that were originally for red wavelengths.

B.8 Radiometer

The radiometers are three model RM3700 radiometers each using an RjP-465 Energy Probe (both from www.laserprobe.com). The device can measure energy pulses from the laser.

The device communicates with the calibration control computer via a usb-serial cable and the PySerial python module.

This device has two modes for communicating energy measurements, an Analog Data mode (AD mode) and a Fast Data mode (FD Mode). The AD mode is unable to report energy measurements at 500Hz due to the limitations of the onboard chip, while in FD mode, each energy measurement is packed into two bytes, and then sent to the calibration control computer, which then decodes them with the DecodeFDDataPack() function the RM3700.py driver.

Through the normal remote operation of the RM3700, the front display constantly goes blank.

The effective range may be one order of magnitude below the manufacturer's specifications.

B.9 LabJack DAQ Board

A small DAQ board that plugs into the calibration control computer via USB. It has a small thermometer inside, and the temperature measurement only has a resolution of about 0.1°. It is also hooked up to a small voltage divider that can be used to monitor the laser voltage.